

Enhanced T_c in eutectic high-entropy alloy superconductors Hf-Nb-Sc-Ti-Zr

Issei Kubo^a, Yuto Watanabe^b, Shuma Kawashima^a, Tomohiro Miyaji^a,
Yoshikazu Mizuguchi^b, Terukazu Nishizaki^c, Jiro Kitagawa^a

^a*Department of Electrical Engineering, Faculty of Engineering, Fukuoka Institute of Technology, 3-30-1 Wajiro-higashi, Higashi-ku, Fukuoka, 811-0295, Japan*

^b*Department of Physics, Tokyo Metropolitan University, Hachioji, 192-0397, Japan*

^c*Department of Electrical Engineering, Faculty of Science and Engineering, Kyushu Sangyo University, 2-3-1 Matsukadai, Higashi-ku, Fukuoka, 813-8503, Japan*

Abstract

The present investigation into the superconducting properties of eutectic high-entropy alloy (HEA) Hf-Nb-Sc-Ti-Zr systems reveals an enhanced superconducting critical temperature (T_c) in body-centered cubic (bcc) phases compared to typical quinary bcc HEAs. In Hf₁₀Nb₂₅Sc₂₅Ti₂₀Zr₂₀, Hf₅Nb₄₅Sc₂₀Ti₁₅Zr₁₅, and Hf₅Nb₄₅Sc₁₀Ti₅Zr₃₅ systems, which span a broad range of valence electron concentration per atom, lattice strain and the presence of partial or absent eutectic phases are characteristic features at lower annealing temperatures. The eutectic regions expand rapidly following annealing at 600 °C in all systems. The T_c of each system increases markedly with rising annealing temperatures from 400 °C to 600 °C, reaching a maximum value of 9.93 K in the Hf₅Nb₄₅Sc₁₀Ti₅Zr₃₅ sample annealed at 800 °C. Nearly all samples can be classified as strong-coupling superconductors. The sample annealed at 500 °C in the Hf₅Nb₄₅Sc₁₀Ti₅Zr₃₅ system exhibits a critical current density (J_c) exceeding the practical threshold of 10⁵ A/cm² up to approximately 4 T at 4.2 K and 6 T at 2 K. The elevated J_c is attributed to significant lattice strain and phase instability. The underlying mechanism for the enhanced T_c in Hf-Nb-Sc-Ti-Zr systems is examined through specific heat data analysis, suggesting that the expansion of the eutectic regions induced by thermal annealing plays a pivotal role.

Keywords: Metals and alloys, Multicomponent, Superconductivity, Eutectic structure, High-entropy alloys

1. Introduction

High-entropy alloys (HEAs) challenge traditional alloy design paradigms, wherein a few minor elements are incorporated into one or two primary constituents to enhance specific properties. The foundational principle of HEA design is the formation of solid solution phases stabilized by high configurational entropy[1, 2, 3, 4]. Consequently, HEAs represent an emerging class of multicomponent alloys comprising four or more principal elements[5]. These alloys exhibit various functionalities, including exceptional mechanical performance at elevated temperatures, superior corrosion resistance, wear-resistant hard coatings, and soft ferromagnetism, underscoring their growing importance in materials science[6, 7, 8, 9, 10]. A particularly notable feature of HEAs—rarely observed in conventional alloys—is their multifunctionalities, such as the simultaneous realization of high strength and ductility or the coexistence of soft ferromagnetism and corrosion resistance[11, 12, 13]. The demand for such advanced materials is increasing across critical sectors, including aerospace, nuclear energy, and defense.

Superconductivity is a key functional property of metallic alloys, and research into HEA superconductors has advanced significantly over the past decade[14, 15, 16, 17, 18, 19]. Notably, the discovery of robust superconductivity under extreme conditions—such as high pressure and ion irradiation—and the observation of high critical current density (J_c) in HEA thin films are considered groundbreaking developments[20, 21, 22]. Multifunctionality is also anticipated in HEA superconductors, for instance, as superconducting wires suitable for aerospace or nuclear fusion applications. With a focus on body-centered cubic (bcc) alloy superconductors, conventional binary or ternary d -electron alloys exhibit the well-known Matthias rule, which correlates the superconducting critical temperature (T_c) with valence electron concentration per atom (VEC), showing broad maxima at VEC values near 4.6 and 6.6[23]. This rule has also been examined in numerous quinary bcc HEA superconductors within the VEC range of 4.1–5.2[24]. Although quinary HEAs tend to exhibit Matthias rule-like behavior, their T_c values are significantly suppressed compared to conventional bcc alloys with equivalent VEC, likely due to the pronounced structural disorder inherent to HEAs.

We have recently reported the eutectic HEA superconductor NbScTiZr, which exhibits a distinctive annealing temperature dependence of T_c and an intriguing correlation between microstructure and J_c [25, 26]. The eutectic structure of NbScTiZr comprises bcc and hexagonal close-packed (hcp)

phases. Pioneering work by Krnel et al. revealed that the bcc phase undergoes a superconducting transition in the as-cast state[27]. Detailed investigations by our research group into the effects of annealing on the superconducting properties of NbScTiZr demonstrated a marked enhancement of T_c from 7.9 K in the as-cast state to 9 K in the sample annealed at 800 °C[25, 26]. Structural characterization indicates the presence of lattice strain at lower annealing temperatures, corroborated by a reduction in the lattice parameter. The as-cast sample exhibits a fine eutectic lamellar-like structure with a thickness of approximately 70 nm. While this fine structure is preserved in the sample annealed at 400 °C, further increases in annealing temperature lead to significant grain coarsening. An additional key feature of NbScTiZr is its elevated J_c ; the sample annealed at 400 °C achieves peak performance, exceeding the practical threshold of 10^5 A/cm² up to approximately 3.5 T at 4.2 K and 5.5 T at 2 K[19]. The high performance is attributed to the combined effects of pronounced lattice strain and the fine eutectic microstructure.

Notably, NbScTiZr samples, from the as-cast to 800 °C annealed states, exhibit a significant deviation from the Matthias rule-like behavior observed in many bcc HEAs; specifically, T_c is enhanced[25, 26]. According to BCS theory, T_c depends on two principal factors: the density of states at the Fermi level (E_F), denoted as $D(E_F)$, and the electron-phonon interaction. The VEC reflects $D(E_F)$, and the Matthias rule is predicated on the assumption that $D(E_F)$ primarily governs T_c [23]. Consequently, the deviation observed in NbScTiZr implies that the eutectic structure may significantly influence the electron-phonon interaction. To evaluate the universality of this deviation from the typical trend observed in bcc HEAs, it is desirable to investigate quinary HEAs with eutectic microstructures, as many bcc superconducting HEAs are quinary in composition. Moreover, we aim to explore the relationship between microstructure and J_c in quinary eutectic HEAs.

In this study, we incorporated the element Hf into the NbScTiZr matrix, preparing the eutectic alloy systems $\text{Hf}_{10}\text{Nb}_{25}\text{Sc}_{25}\text{Ti}_{20}\text{Zr}_{20}$, $\text{Hf}_5\text{Nb}_{45}\text{Sc}_{20}\text{Ti}_{15}\text{Zr}_{15}$, and $\text{Hf}_5\text{Nb}_{45}\text{Sc}_{10}\text{Ti}_5\text{Zr}_{35}$, which span a wide range of VEC values. We systematically investigated the structural, metallurgical, and superconducting properties of these systems under varying annealing conditions. The comparison of superconducting properties among quinary bcc HEA superconductors was discussed through the VEC dependence of T_c and specific heat data analyses.

2. Materials and Methods

The as-cast polycrystalline samples were synthesized using a homemade arc furnace under an argon atmosphere. The constituent elements were Hf chips (Mitsuwa Chemicals, 99.6 %), Nb wire (Nilaco, 99.9 %), Sc chips (Kojundo Chemical Laboratory, 99 %), Ti wire (Nilaco, 99.9 %), and Zr wire (Nilaco, 99.5 %). Elemental mixtures with atomic ratios of Hf:Nb:Sc:Ti:Zr = 10:25:25:20:20, 5:45:20:15:15, or 5:45:10:5:35 were repeatedly melted with intermediate flipping to ensure homogeneity, followed by quenching on a water-cooled copper hearth. The nominal compositions were selected to span a broad range of VEC. The as-cast samples were sealed in evacuated quartz tubes and subjected to annealing at 400 °C, 500 °C, 600 °C, or 800 °C for four days using an electric furnace. The annealing temperatures of 400 °C, 600 °C, and 800 °C were adopted in accordance with our previous study[26], while an additional condition of 500 °C was introduced to examine the detailed annealing-temperature dependence of the lattice parameter of the bcc phase. No mechanical deformation (e.g., rolling) was applied during sample preparation.

Room-temperature X-ray diffraction (XRD) patterns were collected using a Shimadzu XRD-7000L diffractometer equipped with Cu-K α radiation in Bragg-Brentano geometry. Due to the difficulty in producing fine powders, thin slabs sectioned from the bulk samples were used. Microstructural observations were conducted via field-emission scanning electron microscopy (FE-SEM, JEOL JSM-7100F). Elemental compositions were analyzed using an energy-dispersive X-ray (EDX) spectroscopy system integrated with the FE-SEM. The microstructures were observed on the polished surfaces. For the microstructural observation and EDX analysis, the sample surfaces were sequentially polished using silicon carbide papers (#240, #400, #600, and #1000 mesh), alumina pastes (5, 1, and 0.1 μm), and colloidal silica (0.04 μm).

The temperature dependence of the dc magnetization $M(T)$ and the isothermal magnetization curves were measured using a SQUID magnetometer (MPMS3, Quantum Design). For the $M(T)$ measurements, the sample was first cooled below T_c in zero field, after which an external magnetic field of 0.4 mT was applied, and M was measured during warming (zero-field-cooled warming protocol). Subsequently, the sample was cooled again below T_c under a 0.4 mT field, and M was measured during warming (field-cooled warming protocol). The isothermal magnetization curves were obtained un-

der external magnetic fields sweeping between -7 T and 7 T. Temperature-dependent electrical resistivity $\rho(T)$ measurements under magnetic fields of 0, 0.5, 1, 2, 3, 4, 5, 6, 7, 8, and 9 T were performed using the standard four-probe technique with a PPMS system (Quantum Design). Specific heat C_p was measured using the thermal-relaxation method, also employing the PPMS apparatus.

3. Results and Discussion

3.1. Structural and Metallographic Characterizations

Figures 1(a)-(c) present the XRD patterns of all investigated samples. In the $\text{Hf}_{10}\text{Nb}_{25}\text{Sc}_{25}\text{Ti}_{20}\text{Zr}_{20}$ and $\text{Hf}_5\text{Nb}_{45}\text{Sc}_{20}\text{Ti}_{15}\text{Zr}_{15}$ alloy systems, the Bragg reflection peaks observed in the as-cast samples can be attributed to either the bcc (*) or hcp (+) phases. In both systems, the intensity of the hcp phase increases progressively from the as-cast state to the 600 °C annealed condition. Concomitant with this evolution, the Bragg peaks of the bcc phase systematically shift to higher angles, indicating a significant reduction in the lattice parameter (see Figs. 1(a) and (b)). In contrast, the XRD pattern of the as-cast $\text{Hf}_5\text{Nb}_{45}\text{Sc}_{10}\text{Ti}_5\text{Zr}_{35}$ exhibits a single-phase bcc structure, which is preserved in the sample annealed at 400 °C, although with broadened diffraction peaks. Further elevation of the annealing temperature results in the emergence of the hcp phase alongside the bcc phase, accompanied by a pronounced shift of the bcc Bragg reflections toward higher angles. Upon assigning Miller indices to the observed Bragg peaks, the lattice parameters of both phases were calculated using the least-squares method. Table 1 summarizes the resulting lattice parameters for all phases across the different systems. The annealing-temperature dependence of the bcc lattice parameters is plotted in Fig. 1(d), where the as-cast state is treated as the 0 °C annealing. In each alloy system, the lattice parameter exhibits a sharp decrease above approximately 400 °C, reaching a minimum at 500-600 °C. This behavior mirrors that observed in the eutectic NbScTiZr system and is attributed to thermally induced lattice strain[25, 26]. It is also noteworthy that similar lattice parameter contraction upon thermal annealing has been reported in $\text{Ta}_{1/6}\text{Nb}_{2/6}\text{Hf}_{1/6}\text{Zr}_{1/6}\text{Ti}_{1/6}$ and $(\text{TaNb})_{0.7}(\text{HfZrTi})_{0.5}$ [28, 29].

Figures 2(a)-(e) display SEM images of $\text{Hf}_{10}\text{Nb}_{25}\text{Sc}_{25}\text{Ti}_{20}\text{Zr}_{20}$ samples subjected to various annealing treatments. The chemical compositions determined by EDX for all samples are summarized in Table 1. A dendritic microstructure is observed in the as-cast sample (Fig. 2(a)). The VEC of

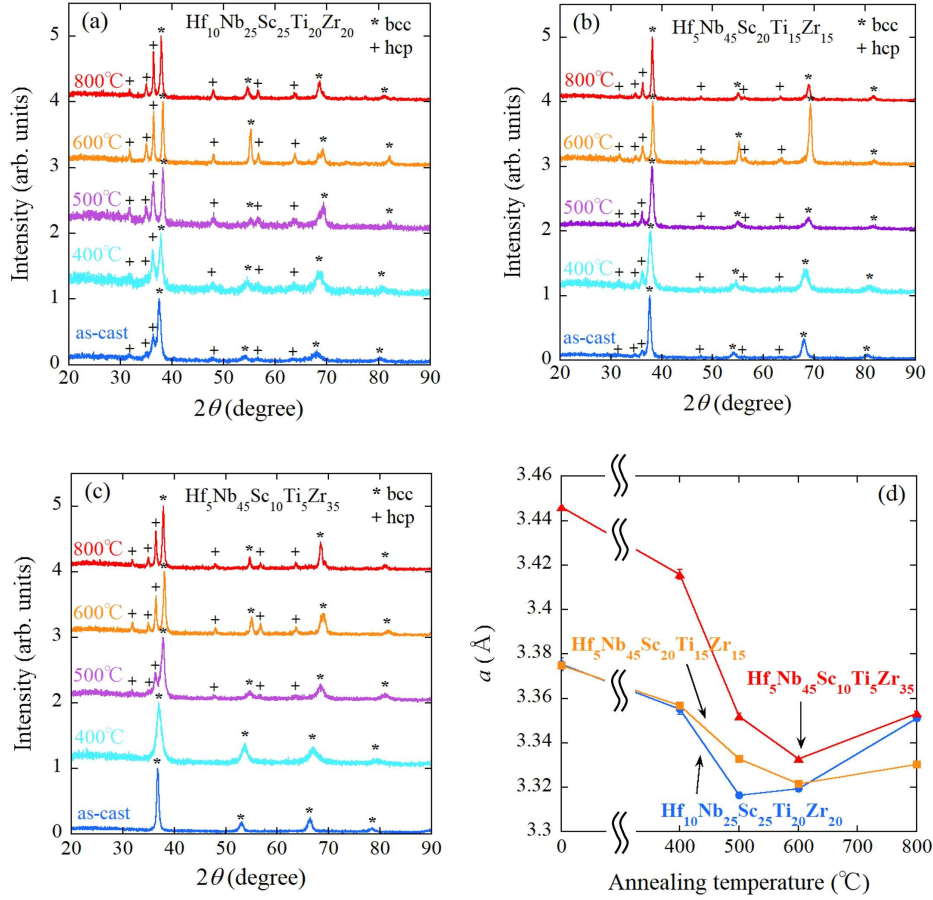


Figure 1: XRD patterns of (a) $\text{Hf}_{10}\text{Nb}_{25}\text{Sc}_{25}\text{Ti}_{20}\text{Zr}_{20}$, (b) $\text{Hf}_5\text{Nb}_{45}\text{Sc}_{20}\text{Ti}_{15}\text{Zr}_{15}$, and (c) $\text{Hf}_5\text{Nb}_{45}\text{Sc}_{10}\text{Ti}_5\text{Zr}_{35}$ samples prepared under various annealing conditions. The origin of each XRD pattern is vertically offset for the clarity. (d) Dependence of lattice parameter on annealing temperature for $\text{Hf}_{10}\text{Nb}_{25}\text{Sc}_{25}\text{Ti}_{20}\text{Zr}_{20}$, $\text{Hf}_5\text{Nb}_{45}\text{Sc}_{20}\text{Ti}_{15}\text{Zr}_{15}$, and $\text{Hf}_5\text{Nb}_{45}\text{Sc}_{10}\text{Ti}_5\text{Zr}_{35}$ systems.

Table 1: Chemical compositions of bcc and hcp phases, lattice parameters, and VEC of prepared samples.

sample	composition	lattice parameter (Å)	VEC
Hf ₁₀ Nb ₂₅ Sc ₂₅ Ti ₂₀ Zr ₂₀	as-cast	bcc:Hf _{12.2(1)} Nb _{28.9(3)} Sc _{20.2(7)} Ti _{19.0(3)} Zr _{19.7(5)}	a=3.375(3) 4.09
	400 °C	hcp:Hf _{8.8(2)} Nb _{19.3(4)} Sc _{33.3(4)} Ti _{18.3(3)} Zr _{20.3(2)}	a=3.251(1), c=5.133(2) 3.86
		bcc:Hf _{12.5(3)} Nb _{30.1(7)} Sc _{19.0(6)} Ti _{19.1(3)} Zr _{19.3(2)}	a=3.355(2) 4.11
	500 °C	hcp:Hf _{9.4(2)} Nb _{20.7(5)} Sc _{31.1(5)} Ti _{18.6(2)} Zr _{20.1(3)}	a=3.250(1), c=5.132(2) 3.90
		bcc:Hf _{12.7(1)} Nb _{31.6(5)} Sc _{17.4(5)} Ti _{19.7(3)} Zr _{18.5(5)}	a=3.316(1) 4.14
	600 °C	hcp:Hf _{9.3(9)} Nb ₂₀₍₁₎ Sc ₃₁₍₁₎ Ti _{19.0(9)} Zr _{20.2(5)}	a=3.246(1), c=5.124(2) 3.89
		bcc:Hf _{9.4(3)} Nb _{35.3(4)} Sc _{15.9(8)} Ti _{25.1(3)} Zr _{14.2(4)}	a=3.319(1) 4.19
	800 °C	hcp:Hf _{11.3(5)} Nb ₂₀₍₁₎ Sc ₂₉₍₁₎ Ti ₁₇₍₁₎ Zr ₂₃₍₁₎	a=3.242(1), c=5.117(2) 3.91
		bcc:Hf _{10.3(1)} Nb ₃₆₍₁₎ Sc ₁₄₍₁₎ Ti _{25.0(7)} Zr _{14.7(9)}	a=3.351(1) 4.22
	hcp:Hf _{11.5(1)} Nb _{17.2(3)} Sc _{32.8(3)} Ti _{14.7(3)} Zr _{23.8(2)}	a=3.246(1), c=5.117(2) 3.84	
Hf ₅ Nb ₄₅ Sc ₂₀ Ti ₁₅ Zr ₁₅	as-cast	bcc:Hf _{5.7(1)} Nb ₅₃₍₁₎ Sc _{11.7(9)} Ti _{16.0(6)} Zr _{13.1(4)}	a=3.375(2) 4.42
	400 °C	hcp:Hf _{4.9(3)} Nb ₂₁₍₁₎ Sc ₄₄₍₁₎ Ti _{10.6(4)} Zr ₂₀₍₁₎	a=3.268(1), c=5.166(2) 3.77
		bcc:Hf _{5.4(1)} Nb ₅₇₍₁₎ Sc _{10.1(5)} Ti _{15.5(8)} Zr _{12.0(4)}	a=3.357(1) 4.47
	500 °C	hcp:Hf _{4.4(1)} Nb ₁₈₍₁₎ Sc ₅₁₍₁₎ Ti _{8.5(7)} Zr _{17.9(7)}	a=3.264(1), c=5.159(1) 3.67
		bcc:Hf _{5.8(1)} Nb _{59.4(5)} Sc _{8.2(3)} Ti _{14.8(2)} Zr _{11.7(1)}	a=3.333(1) 4.51
	600 °C	hcp:Hf _{4.5(2)} Nb ₁₉₍₁₎ Sc ₄₉₍₁₎ Ti _{9.3(6)} Zr _{18.2(2)}	a=3.270(2), c=5.151(4) 3.70
		bcc:Hf _{5.7(3)} Nb _{52.9(1)} Sc _{12.1(1)} Ti _{16.5(3)} Zr _{12.8(5)}	a=3.322(1) 4.41
	800 °C	hcp:Hf _{4.6(2)} Nb ₂₀₍₁₎ Sc ₄₈₍₁₎ Ti _{8.2(1)} Zr _{19.2(1)}	a=3.258(1), c=5.139(2) 3.72
		bcc:Hf _{5.1(1)} Nb ₅₆₍₁₎ Sc ₁₀₍₁₎ Ti _{18.0(5)} Zr _{10.6(6)}	a=3.330(1) 4.46
	hcp:Hf _{6.8(2)} Nb ₁₀₍₁₎ Sc _{47.8(8)} Ti _{5.8(2)} Zr _{29.2(5)}	a=3.260(1), c=5.144(2) 3.62	
Hf ₅ Nb ₄₅ Sc ₁₀ Ti ₅ Zr ₃₅	as-cast	bcc (bright):Hf _{5.9(1)} Nb ₅₀₍₁₎ Sc ₇₍₁₎ Ti _{4.7(2)} Zr ₃₂₍₁₎	a=3.446(1) 4.43
	400 °C	bcc (dark):Hf _{5.4(2)} Nb ₃₈₍₁₎ Sc ₁₃₍₁₎ Ti _{5.1(4)} Zr _{38.8(9)}	a=3.446(1) 4.25
		bcc (bright):Hf _{6.1(1)} Nb _{51.8(5)} Sc _{6.0(4)} Ti _{4.8(4)} Zr _{31.2(7)}	a=3.416(2) 4.46
	500 °C	bcc (dark):Hf _{5.4(2)} Nb ₃₈₍₁₎ Sc _{12.6(8)} Ti _{5.3(3)} Zr ₃₉₍₁₎	a=3.416(2) 4.25
		bcc (bright):Hf _{5.9(3)} Nb _{48.3(4)} Sc _{7.9(1)} Ti _{4.8(3)} Zr _{33.2(3)}	a=3.352(1) 4.40
	600 °C	bcc (dark):Hf _{5.6(2)} Nb ₃₉₍₁₎ Sc _{12.0(5)} Ti _{5.2(4)} Zr _{37.8(9)}	a=3.352(1) 4.27
		hcp: not identified due to fine microstructure	a=3.251(3), c=5.128(6) -
	800 °C	bcc (bright):Hf _{6.2(3)} Nb _{55.8(1)} Sc _{5.7(2)} Ti _{4.0(2)} Zr _{28.4(2)}	a=3.333(1) 4.50
		bcc (dark):Hf _{5.5(2)} Nb ₃₆₍₁₎ Sc ₁₄₍₁₎ Ti _{5.0(3)} Zr ₃₉₍₁₎	a=3.333(1) 4.22
	hcp: not identified due to fine microstructure	a=3.241(1), c=5.126(2) -	
bcc:Hf _{4.6(3)} Nb ₆₅₍₁₎ Sc ₃₍₁₎ Ti _{6.6(3)} Zr ₂₁₍₁₎	a=3.353(1) 4.62		
hcp:Hf _{6.5(2)} Nb ₁₄₍₁₎ Sc _{23.3(1)} Ti _{2.7(1)} Zr ₅₄₍₁₎	a=3.239(1), c=5.135(2) 3.91		

the bright dendritic phase exceeds 4.0, whereas the interdendritic dark phase exhibits a VEC below 4.0 (see also Table 1). According to the phase stability study of alloys containing Sc and group 4 and 5 elements, the bcc and hcp phases are stabilized at VEC values above and below 4.0, respectively[30]. This VEC–structure relationship has also been confirmed in NbScTiZr[25], supporting the interpretation that the bright and dark phases correspond to the bcc and hcp structures, respectively. A magnified image (Fig. 2(b)) reveals a weave-like microstructure. Notably, a characteristic line, marked by red arrows, runs along the grain boundaries between the bcc and hcp phases and is accompanied by a lamellar-like structure. Annealing at 400 °C does not significantly alter the microstructure, although more pronounced lamellar features with spacings of approximately 80 nm partially emerge within grains in the 500 °C annealed sample (see Figs. S1(a)-(e) in the Supplementary Material). At 600 °C, both bcc and hcp phases are filled with a eutectic microstructure, as revealed by the high-magnification image ($\times 6000$, Fig. 2(d)). The lower-magnification image of the 800 °C annealed sample (Fig. 2(e)) also exhibits a developed eutectic structure and evidence of grain coarsening compared to the 600 °C sample. The VEC of the bcc phase increases systematically with annealing temperature, as listed in Table 1, which originates from a compositional shift toward a (Nb,Ti)-rich and Zr-poor state relative to the as-cast condition.

In the SEM image of the as-cast $\text{Hf}_5\text{Nb}_{45}\text{Sc}_{20}\text{Ti}_{15}\text{Zr}_{15}$ sample, the large bright grains are assigned to the bcc phase based on the VEC–phase relationship (Fig. 3(a) and Table 1). A eutectic structure is discernible between the large bcc grains. This morphology is retained in the 400 °C and 500 °C annealed samples (Fig. S2 in the Supplementary Material and Fig. 3(b)). Annealing at 600 °C induces a fine eutectic structure within the primary bcc phase (Figs. 3(c) and (d)). The grain size of the eutectic structure increases upon annealing at 800 °C, as shown in Fig. 3(e). The annealing effect on the VEC of the bcc phase in $\text{Hf}_5\text{Nb}_{45}\text{Sc}_{20}\text{Ti}_{15}\text{Zr}_{15}$ is negligible, as indicated in Table 1.

Although the XRD pattern of the as-cast $\text{Hf}_5\text{Nb}_{45}\text{Sc}_{10}\text{Ti}_5\text{Zr}_{35}$ sample suggests a single-phase bcc structure, the corresponding SEM image reveals a phase-segregated microstructure ((Fig. 4(a)). Table 1 lists the chemical compositions of both the bright and dark regions, with VEC values of 4.43 and 4.25, respectively—consistent with those stabilizing bcc HEAs[30]. Thus, the as-cast state is described as a dual bcc-phase structure with slightly differing VECs. The 400 °C annealed sample maintains a similar microstructure (see

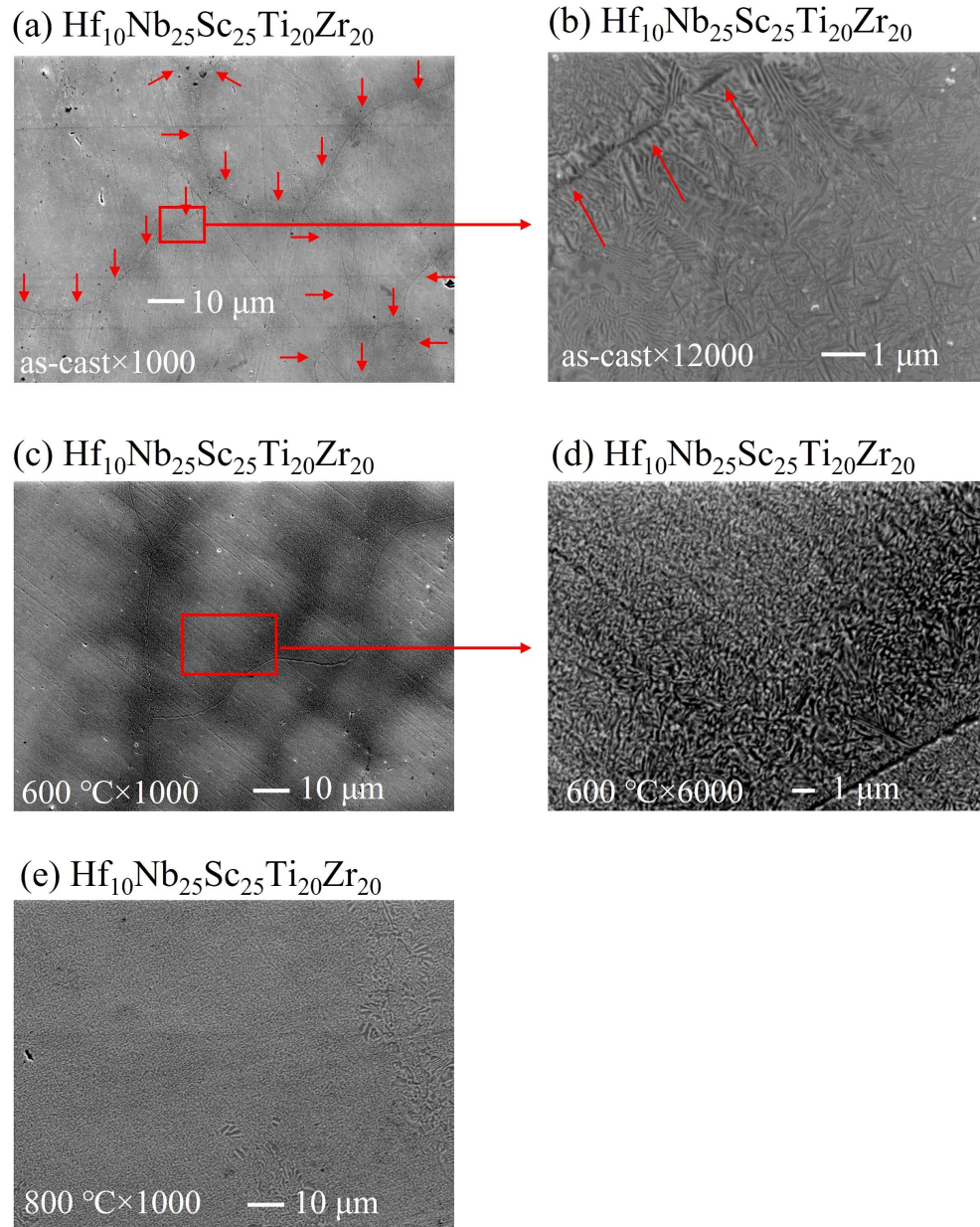


Figure 2: SEM images of $\text{Hf}_{10}\text{Nb}_{25}\text{Sc}_{25}\text{Ti}_{20}\text{Zr}_{20}$ for as-cast sample (a) and (b) and heat-treated samples at (c) and (d) 600 °C, and (e) 800 °C, respectively.

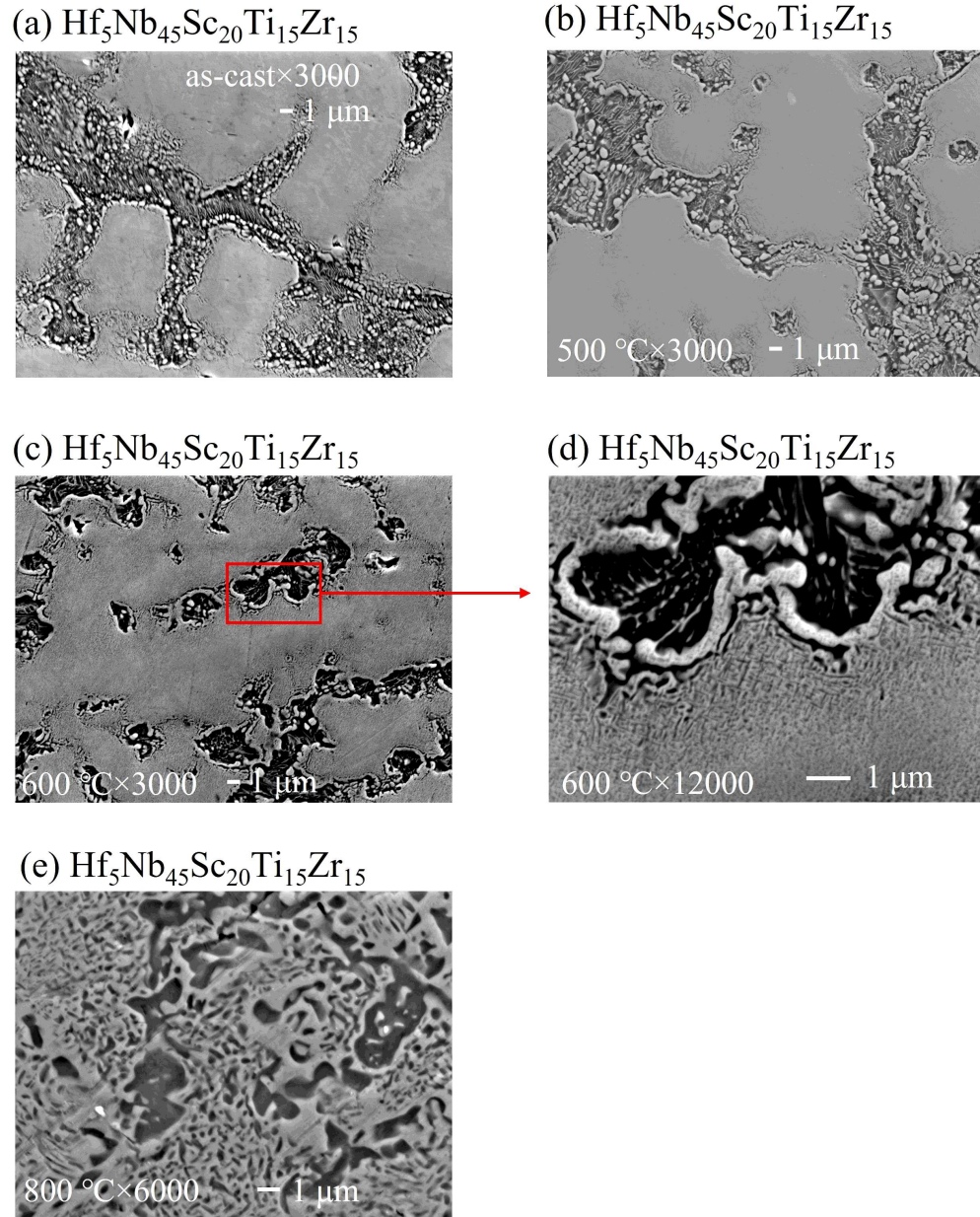


Figure 3: SEM images of $\text{Hf}_5\text{Nb}_{45}\text{Sc}_{20}\text{Ti}_{15}\text{Zr}_{15}$ for as-cast sample (a) and heat-treated samples at (b) 500°C , (c) and (d) 600°C , and (e) 800°C , respectively.

Fig. S3 in the Supplementary Material). In the 500 °C annealed sample, subtle microstructural evolution is observed (Figs. 4(b) and (c)), with very fine eutectic structures, approximately 40 nm in spacing, appearing in some dark regions. This microstructural change aligns with the emergence of hcp reflections in the XRD pattern (see also Fig. 1(c)). At 600 °C, fine eutectic structures also appear in the bright regions (Figs. 4(d) and (e)). Figure 4(f) illustrates the overall grain coarsening following 800 °C annealing. Due to the extremely fine eutectic features, determining the precise chemical composition of the hcp phase in the 500 °C and 600 °C annealed samples was challenging. Therefore, the compositions of the bright and dark regions in Figs. 4(b) and (d) are reported in Table 1. While the VEC values of the bright and dark phases remain unchanged from the as-cast to the 500 °C annealed states, a systematic slight increase in the VEC of the bright phase is observed at 600 °C and 800 °C. This increase results from compositional changes trending toward Nb-rich and Zr-deficient compositions with increasing annealing temperature.

3.2. Magnetization, electrical resistivity, and specific heat

Figures 5(a), (c), and (e) summarize the temperature-dependent magnetization $M(T)$ and electrical resistivity $\rho(T)$ for all systems. $M(T)$ was measured under an external field $\mu_0 H$ (μ_0 : the vacuum permeability) of 0.4 mT. In the figures, ZFC and FC refer to the zero-field-cooled and field-cooled measurement protocols. $\rho(T)$ data were acquired under zero external magnetic field. We confirmed the presence of a diamagnetic signal and zero resistivity in each sample. Although the onset temperature of superconductivity in $\rho(T)$ tends to be higher than that observed in ZFC $M(T)$, Figs. S4(a)-(c), which present ZFC $M(T)$ on an expanded scale in the Supplementary Material, demonstrate good agreement in the onset temperature between $\rho(T)$ and $M(T)$ for most samples. The specific heat C_p data for all samples are plotted as a function of temperature in Figs. 5(b), (d), and (f).

As shown in Fig. 5(a), T_c of $\text{Hf}_{10}\text{Nb}_{25}\text{Sc}_{25}\text{Ti}_{20}\text{Zr}_{20}$ slightly increases from the as-cast state to the sample annealed at 400 °C and is markedly enhanced upon heat treatment at 500 °C. T_c reaches its maximum in the sample annealed at 600 °C, followed by a slight decrease after annealing at 800 °C (see Fig. 5(a) and Fig. 6(a)). The C_p data for each $\text{Hf}_{10}\text{Nb}_{25}\text{Sc}_{25}\text{Ti}_{20}\text{Zr}_{20}$ sample indicate the bulk nature of the superconducting transition (Fig. 5(b)). The agreement among the transition temperatures determined from C_p , M , and ρ measurements is relatively satisfactory for the samples annealed at 500 °C,

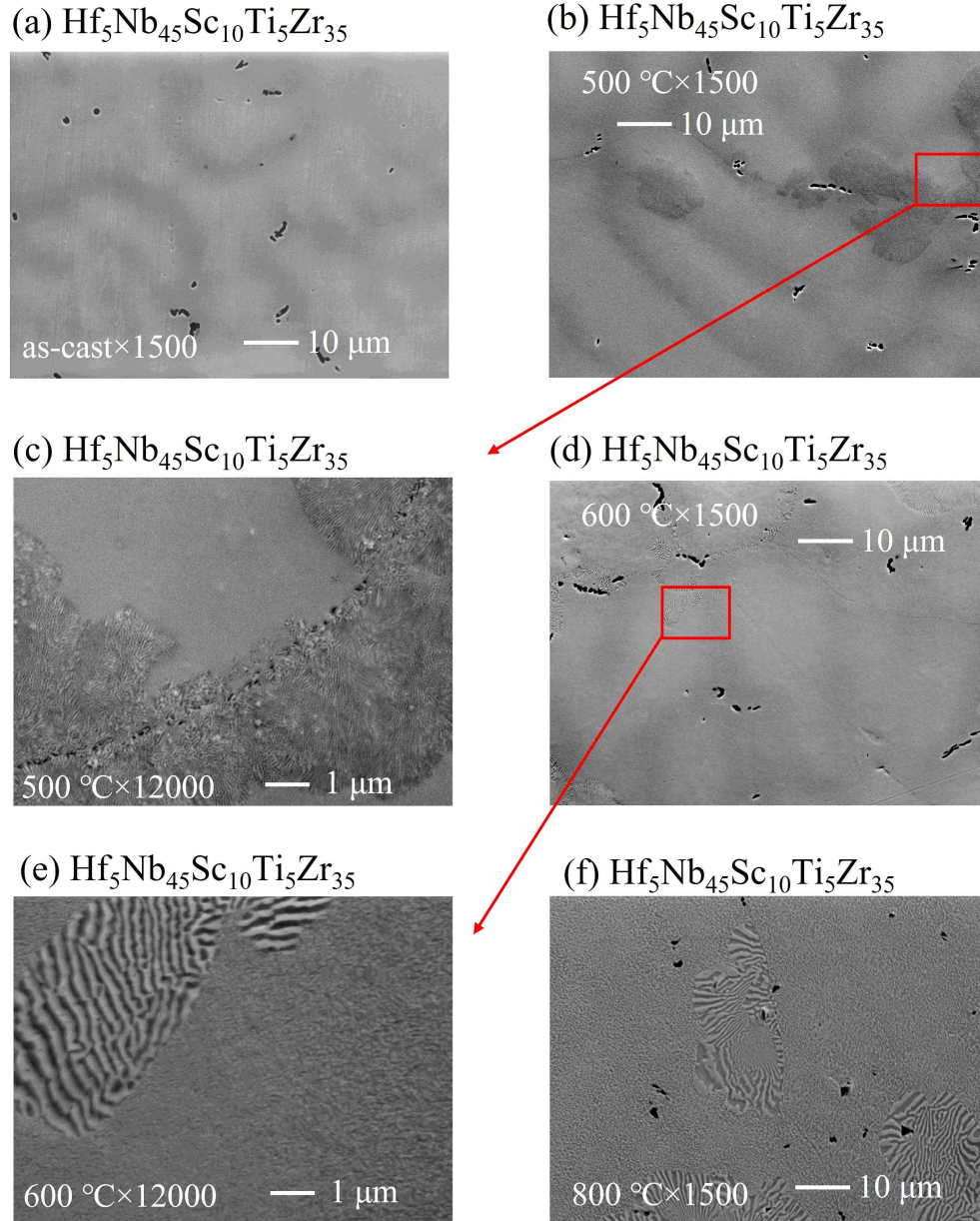


Figure 4: SEM images of $\text{Hf}_5\text{Nb}_{45}\text{Sc}_{10}\text{Ti}_5\text{Zr}_{35}$ for as-cast sample (a) and heat-treated samples at (b) and (c) 500 $^\circ\text{C}$, (d) and (e) 600 $^\circ\text{C}$, and (f) 800 $^\circ\text{C}$, respectively.

600 °C, and 800 °C. In contrast, for the as-cast and 400 °C-annealed samples, the onset temperature of the superconducting transition observed in ρ or M is 2–3 K higher than that in C_p . To investigate this discrepancy, the temperature dependence of the electronic specific heat $C_{el}(T)$ was obtained by subtracting the phonon contribution represented by βT^3 , and the resulting $C_{el}(T)/\gamma T$ (γ : electronic specific heat coefficient) was compared with $\rho(T)$ and $M(T)$, as shown in Figs. S5(a) and (b) of the Supplementary Material. This comparison reveals that a weak anomaly in $C_{el}(T)/\gamma T$ emerges below the temperature at which $\rho(T)$ or $M(T)$ exhibits a sharp superconducting transition, suggesting an inhomogeneous superconducting state. This hypothesis is supported by SEM images of the as-cast and 400 °C annealed samples. In both, the microstructure is characterized by dendritic bcc and interdendritic hcp phases, with partial eutectic regions present along grain boundaries. As discussed later, the eutectic structure contributes to the enhancement of T_c . Furthermore, the weave-like microstructure within the bcc phase may act as a precursor to eutectic formation, as thermal annealing promotes eutectic development within the bcc matrix. Therefore, the partial eutectic structure and weave-like microstructure likely contribute to the gradual enhancement of T_c , manifested as the weak anomaly in $C_{el}(T)/\gamma T$ observed at 5–7 K.

Although the T_c of $\text{Hf}_5\text{Nb}_{45}\text{Sc}_{20}\text{Ti}_{15}\text{Zr}_{15}$ remains nearly unchanged between the as-cast state and the 400 °C-annealed sample, an increase in the annealing temperature from 400 °C to 600 °C induces a systematic enhancement of T_c (Fig. 5(c) and Fig. 6(b)). Further elevation of the annealing temperature up to 800 °C exerts only a minimal effect on T_c . The annealing temperature dependence of T_c determined by M or ρ measurements is consistent with that derived from $C_p(T)$, all indicating bulk superconducting transitions, as demonstrated in Fig. 5(d). For the $\text{Hf}_5\text{Nb}_{45}\text{Sc}_{10}\text{Ti}_{15}\text{Zr}_{35}$ system, the T_c of the as-cast sample decreases with annealing up to 400 °C before exhibiting a systematic increase with annealing above 400 °C (Fig. 5(e) and Fig. 6(c)). The $M(T)$ curve for the 500 °C annealed sample shows a broad, two-step diamagnetic transition, in contrast to the sharp resistivity drop observed in $\rho(T)$. This distinctive feature is prominently reflected in the $C_p(T)$ data in Fig. 5(f). Unlike other samples exhibiting sharp bulk transitions, the 500 °C annealed sample displays an extremely broad transition. This sample lies near the boundary between phase-segregated bcc phases devoid of eutectic structure and those containing a minor eutectic component, implying the presence of phase instability. Consequently, the

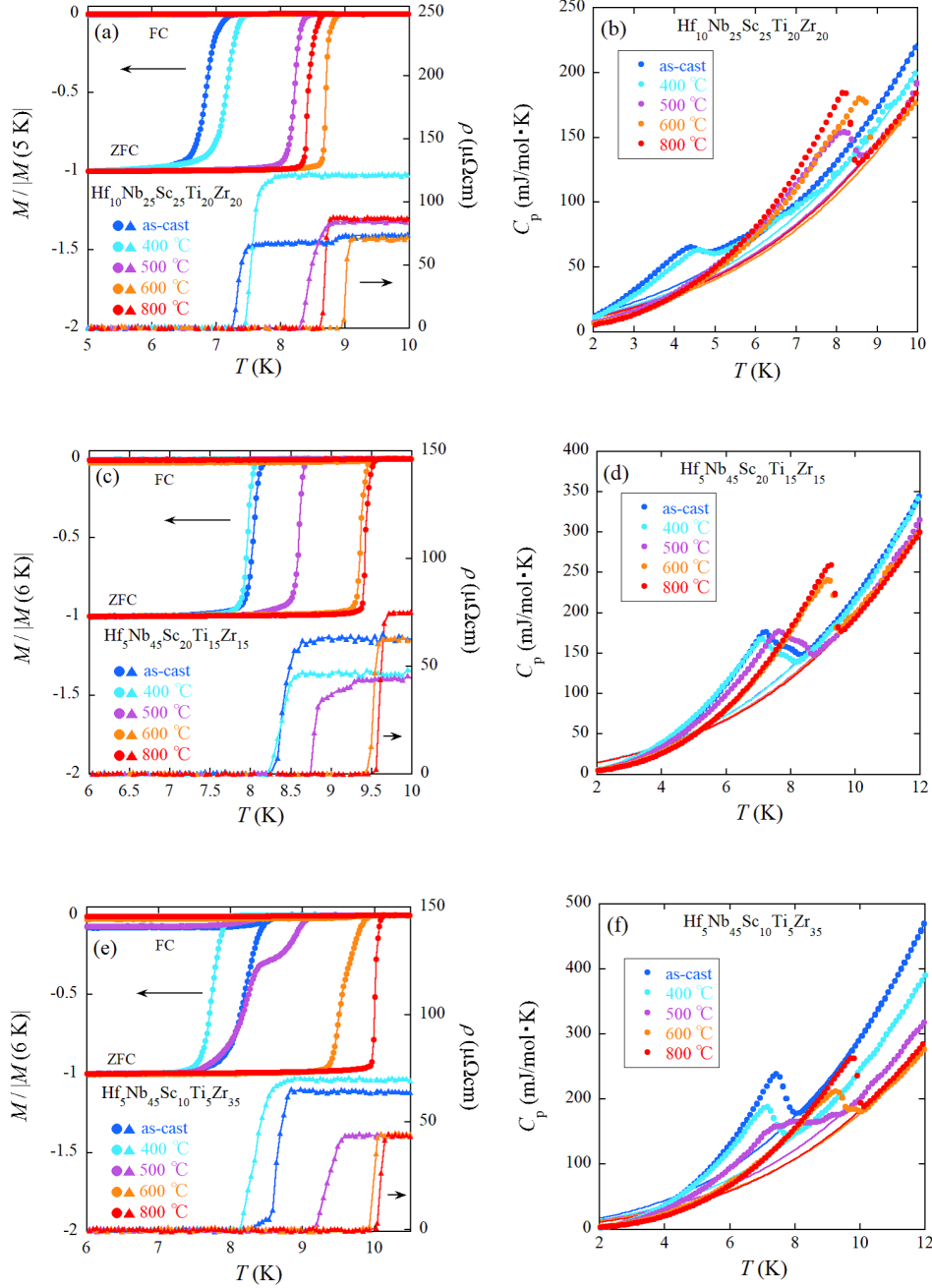


Figure 5: Temperature dependence of M and ρ for (a) $\text{Hf}_{10}\text{Nb}_{25}\text{Sc}_{25}\text{Ti}_{20}\text{Zr}_{20}$, (c) $\text{Hf}_5\text{Nb}_{45}\text{Sc}_{20}\text{Ti}_{15}\text{Zr}_{15}$, and (e) $\text{Hf}_5\text{Nb}_{45}\text{Sc}_{10}\text{Ti}_5\text{Zr}_{35}$ under various annealing conditions. Each M value is normalized to its absolute value at 5 K or 6 K. Plots of C_p versus T for (b) $\text{Hf}_{10}\text{Nb}_{25}\text{Sc}_{25}\text{Ti}_{20}\text{Zr}_{20}$, (d) $\text{Hf}_5\text{Nb}_{45}\text{Sc}_{20}\text{Ti}_{15}\text{Zr}_{15}$, and (f) $\text{Hf}_5\text{Nb}_{45}\text{Sc}_{10}\text{Ti}_5\text{Zr}_{35}$ under various annealing conditions. The solid line in each figure represents the fitting result using $\gamma T + \beta T^3$, where γ is the electronic specific heat coefficient and βT^3 corresponds to the phonon part.

Table 2: T_c , $\mu_0 H_{c1}(0)$, $\mu_0 H_{c2}(0)$, $\xi_{GL}(0)$, $\lambda_{GL}(0)$, κ_{GL} , α_M , λ_{SO} , $\mu_0 H_{c2}^{orb}$, and $\mu_0 H_{c2}^{Pauli}$ of prepared samples. T_c is defined as the midpoint of specific heat jump, except for the as-cast and 400 °C annealed samples of $\text{Hf}_{10}\text{Nb}_{25}\text{Sc}_{25}\text{Ti}_{20}\text{Zr}_{20}$ and the 500 °C annealed sample of $\text{Hf}_5\text{Nb}_{45}\text{Sc}_{10}\text{Ti}_5\text{Zr}_{35}$. For these three samples, T_c is determined by the midpoint of the diamagnetic transition. $\mu_0 H_{c2}^{Pauli}$ is calculated using the relation $1.84T_c^{\rho 50\%}$, where $T_c^{\rho 50\%}$ is the superconducting critical temperature defined by the 50 % criterion of the resistivity drop in the zero-field $\rho(T)$. The sets of $T_c^{\rho 50\%}$ (K) values for the (as-cast, 400 °C, 500 °C, 600 °C, 800 °C) samples are (7.35, 7.56, 8.45, 9.01, 8.68) for $\text{Hf}_{10}\text{Nb}_{25}\text{Sc}_{25}\text{Ti}_{20}\text{Zr}_{20}$, (8.40, 8.37, 8.80, 9.51, 9.60) for $\text{Hf}_5\text{Nb}_{45}\text{Sc}_{20}\text{Ti}_{15}\text{Zr}_{15}$, and (8.65, 8.35, 9.34, 9.98, 10.1) for $\text{Hf}_5\text{Nb}_{45}\text{Sc}_{10}\text{Ti}_5\text{Zr}_{35}$, respectively.

sample	T_c (K)	$\mu_0 H_{c1}(0)$ (mT)	$\mu_0 H_{c2}(0)$ (T)	$\xi_{GL}(0)$ (nm)	$\lambda_{GL}(0)$ (nm)	κ_{GL}	α_M	λ_{SO}	$\mu_0 H_{c2}^{orb}$ (T)	$\mu_0 H_{c2}^{Pauli}$ (T)
$\text{Hf}_{10}\text{Nb}_{25}\text{Sc}_{25}\text{Ti}_{20}\text{Zr}_{20}$										
as-cast	6.83	23.6	12.8	5.1	154	30	1.49	4.0	14.2	13.5
400 °C	7.15	24.7	13.1	5.0	151	30	1.49	4.0	14.6	13.9
500 °C	8.36	25.5	11.5	5.4	146	27	1.76	0.5	19.3	15.5
600 °C	8.75	27.3	13.3	5.0	142	29	1.22	4.0	14.3	16.6
800 °C	8.37	23.6	13.3	5.0	155	31	1.27	4.0	14.4	16.0
$\text{Hf}_5\text{Nb}_{45}\text{Sc}_{20}\text{Ti}_{15}\text{Zr}_{15}$										
as-cast	7.69	18.5	11.4	5.4	176	33	1.16	2.0	12.8	15.5
400 °C	7.64	17.8	11.2	5.4	180	33	1.00	2.0	10.9	15.4
500 °C	8.17	33.1	11.1	5.4	125	23	1.28	0.5	14.7	16.2
600 °C	9.28	32.5	11.0	5.5	126	23	0.93	4.0	11.5	17.5
800 °C	9.39	26.5	10.8	5.5	142	26	0.9	4.0	11.3	17.7
$\text{Hf}_5\text{Nb}_{45}\text{Sc}_{10}\text{Ti}_5\text{Zr}_{35}$										
as-cast	7.73	8.2	12.1	5.2	283	54	1.10	4.0	12.4	15.9
400 °C	7.39	7.0	11.9	5.3	310	59	1.11	4.0	12.1	15.4
500 °C	8.25	36.5	11.7	5.3	118	22	0.80	-	9.7	17.2
600 °C	9.61	31.9	10.0	5.7	126	22	0.65	-	8.4	18.4
800 °C	9.93	26.6	10.8	5.5	142	26	0.68	-	9.0	18.6

broad transition in $C_p(T)$ is likely attributable to this phase instability.

The lower critical field H_{c1} of each sample was evaluated from the isothermal M - H curves at low magnetic fields, as presented in Figs. S6-S8 of the Supplementary Material. The H_{c1} value is defined at the field where the magnetization deviates from the initial linear slope (indicated by a dashed line in each figure). The extracted H_{c1} values are plotted as a function of temperature in Figs. 6(d)-(f) and analyzed using the Ginzburg–Landau expression:

$$H_{c1}(T) = H_{c1}(0) \left(1 - \left(\frac{T}{T_c} \right)^2 \right), \quad (1)$$

where $H_{c1}(0)$ denotes the lower critical field at zero temperature. All derived parameters are summarized in Table 2. While thermal annealing exhibits a minimal effect on $H_{c1}(0)$ in the $\text{Hf}_{10}\text{Nb}_{25}\text{Sc}_{25}\text{Ti}_{20}\text{Zr}_{20}$ system, heat treat-

ment above 400 °C tends to enhance $H_{c1}(0)$ in the $\text{Hf}_5\text{Nb}_{45}\text{Sc}_{20}\text{Ti}_{15}\text{Zr}_{15}$ and $\text{Hf}_5\text{Nb}_{45}\text{Sc}_{10}\text{Ti}_5\text{Zr}_{35}$ systems.

Figures 6(g)-(i) summarize the temperature dependence of the upper critical field H_{c2} for all systems, derived from the 50 % resistivity drop criterion in $\rho(T)$ under external magnetic fields ranging from 0 to 9 T (see Figs. S9-S11 in the Supplementary Material). The temperature dependence of $\mu_0 H_{c2}$ is analyzed using the Werthamer–Helfand–Hohenberg (WHH) model[31]:

$$\ln \frac{1}{t} = \left(\frac{1}{2} + \frac{i\lambda_{\text{SO}}}{4\gamma_{\text{WHH}}} \right) \psi \left(\frac{1}{2} + \frac{h + \lambda_{\text{SO}}/2 + i\gamma_{\text{WHH}}}{2t} \right) + \left(\frac{1}{2} - \frac{i\lambda_{\text{SO}}}{4\gamma_{\text{WHH}}} \right) \psi \left(\frac{1}{2} + \frac{h + \lambda_{\text{SO}}/2 - i\gamma_{\text{WHH}}}{2t} \right) - \psi \left(\frac{1}{2} \right), \quad (2)$$

where $t = T/T_c$, λ_{SO} is the spin-orbital scattering parameter, $\gamma_{\text{WHH}} = [(\alpha_{\text{M}}h)^2 - (\lambda_{\text{SO}}/2)^2]^{1/2}$ (α_{M} : Maki parameter), and $\psi(x)$ is the digamma function. In this model, h is defined as

$$h = \frac{4H_{c2}(T)}{\pi^2 T_c (-dH_{c2}(T)/dT)|_{T=T_c}}. \quad (3)$$

Once α_{M} is determined, the orbital-limited upper critical field $\mu_0 H_{c2}^{\text{orb}}$ is evaluated using the expression $\frac{\sqrt{2}\mu_0 H_{c2}^{\text{orb}}}{\mu_0 H_{c2}^{\text{Pauli}}}$, where $\mu_0 H_{c2}^{\text{Pauli}} (=1.84T_c)$ denotes the Pauli limiting field. For this calculation, $T_c^{50\%}$ —the critical temperature determined from the 50 % resistivity drop in zero field— is used (see also the caption of Table 2). Table 2 compiles all estimated parameters. For the 500 °C, 600 °C, 800 °C samples of the $\text{Hf}_5\text{Nb}_{45}\text{Sc}_{10}\text{Ti}_5\text{Zr}_{35}$ system, the WHH model fails to accurately fit the $\mu_0 H_{c2}(T)$ data, as exemplified in Fig. S12 of the Supplementary Material. In these cases, the commonly adopted phenomenological formula $H_{c2}(T) = H_{c2}(0) \left(\frac{1-(T/T_c)^2}{1+(T/T_c)^2} \right)$ provides a better fit to the experimental data. The value of $\mu_0 H_{c2}^{\text{orb}}$ is then calculated via $\mu_0 H_{c2}^{\text{orb}} = -0.693T_c \frac{dH_{c2}(T)}{dT}|_{T=T_c}$ [32]. Comparison of the zero-temperature upper critical field $\mu_0 H_{c2}(0)$ indicates that the Ti-rich $\text{Hf}_{10}\text{Nb}_{25}\text{Sc}_{25}\text{Ti}_{20}\text{Zr}_{20}$ system possesses a relatively high $\mu_0 H_{c2}(0)$, consistent with previous observations in Ti-rich bcc HEAs[33]. Samples of $\text{Hf}_{10}\text{Nb}_{25}\text{Sc}_{25}\text{Ti}_{20}\text{Zr}_{20}$ subjected to annealing below 500 °C exhibit $\alpha_{\text{M}} > \sqrt{2}$, implying that $\mu_0 H_{c2}^{\text{orb}}$ exceeds $\mu_0 H_{c2}^{\text{Pauli}}$. A similar characteristic is reported in NbScTiZr , where lattice strain serves as a strong pinning center, suppressing Cooper pair breaking by the Lorentz force[26]. Given the comparable chemical composition, it is plausible that lattice strain also contributes to the enhancement of $\mu_0 H_{c2}^{\text{orb}}$ in $\text{Hf}_{10}\text{Nb}_{25}\text{Sc}_{25}\text{Ti}_{20}\text{Zr}_{20}$. In contrast, most samples in the $\text{Hf}_5\text{Nb}_{45}\text{Sc}_{20}\text{Ti}_{15}\text{Zr}_{15}$

and $\text{Hf}_5\text{Nb}_{45}\text{Sc}_{10}\text{Ti}_5\text{Zr}_{35}$ systems exhibit relatively lower α_M values, indicating that $\mu_0 H_{c2}(0)$ is governed by $\mu_0 H_{c2}^{\text{orb}}$.

The Ginzburg–Landau coherence length $\xi_{\text{GL}}(0)$ was calculated using the relation $\xi_{\text{GL}}(0) = \sqrt{\frac{\Phi_0}{2\pi\mu_0 H_{c2}(0)}}$, where $\Phi_0 = 2.07 \times 10^{-15}$ Wb is the magnetic flux quantum. The corresponding $\xi_{\text{GL}}(0)$ values are listed in Table 2. The range of 5.0 to 5.7 nm is comparable to typical HEAs (e.g., NbRe–HfZrTi: 6.1 nm[34], $\text{Ta}_{1/6}\text{Nb}_{2/6}\text{Hf}_{1/6}\text{Zr}_{1/6}\text{Ti}_{1/6}$: 5.2 nm[35]). The magnetic penetration depth $\lambda_{\text{GL}}(0)$, determined using $\mu_0 H_{c1}(0) = \frac{\Phi_0}{4\pi\lambda_{\text{GL}}(0)^2} \ln \frac{\lambda_{\text{GL}}(0)}{\xi_{\text{GL}}(0)}$, is also included in Table 2. Consequently, the Ginzburg–Landau parameter $\kappa_{\text{GL}} = \lambda_{\text{GL}}(0)/\xi_{\text{GL}}(0)$ was calculated and tabulated for each sample. All κ_{GL} values exceeding $1/\sqrt{2}$ confirm that the investigated alloy systems are classified as type-II superconductors.

Here, we discuss the relationship between the $C_p(T)$ behavior and the superconducting parameters T_c and $\mu_0 H_{c2}(0)$. Figures 5(b), (d), and (f) indicate that the specific-heat jump at T_c becomes sharper with increasing T_c for a fixed chemical composition, except in the case of $\text{Hf}_5\text{Nb}_{45}\text{Sc}_{10}\text{Ti}_5\text{Zr}_{35}$. For $\text{Hf}_5\text{Nb}_{45}\text{Sc}_{10}\text{Ti}_5\text{Zr}_{35}$, both the as-cast and 400 °C-annealed samples consist solely of a bcc structure, and the degree of inhomogeneity is relatively small, which may account for the sharper specific-heat jump even in the lower- T_c sample. In $\text{Hf}_{10}\text{Nb}_{25}\text{Sc}_{25}\text{Ti}_{20}\text{Zr}_{20}$ and $\text{Hf}_5\text{Nb}_{45}\text{Sc}_{20}\text{Ti}_{15}\text{Zr}_{15}$, the low-temperature-annealed samples with reduced T_c likely exhibit significant inhomogeneity arising from the fine coexistence of bcc and hcp microstructures formed during nonequilibrium solidification. High-temperature annealing generally induces microstructural coarsening and mitigates inhomogeneity, thereby giving rise to a sharper superconducting transition. Thus, the correlation between $C_p(T)$ behavior and T_c is intrinsically linked to the issue of sample homogeneity. Regarding the relationship between $C_p(T)$ behavior and $\mu_0 H_{c2}(0)$, the magnitude of $\mu_0 H_{c2}(0)$ appears independent of sample homogeneity, as reflected in the sharpness of the specific-heat jump (see also Table 2). For instance, although $\text{Hf}_5\text{Nb}_{45}\text{Sc}_{10}\text{Ti}_5\text{Zr}_{35}$ annealed at 500 °C exhibits a considerably broadened $C_p(T)$ transition, $\mu_0 H_{c2}(0)$ remains unaffected. We evaluated $\mu_0 H_{c2}(0)$ from $\rho(T)$, which likely probes regions exhibiting the highest $\mu_0 H_{c2}$ even in inhomogeneous samples. The difference in measurement methodology may therefore account for the insensitivity of $\mu_0 H_{c2}(0)$ to $C_p(T)$ behavior.

Several bcc HEA superconductors fall within the strong-coupling regime, as evidenced by $\frac{2\Delta(0)}{k_B T_c}$ and $\frac{\Delta C_{\text{el}}}{\gamma T_c}$ values exceeding the BCS weak-coupling lim-

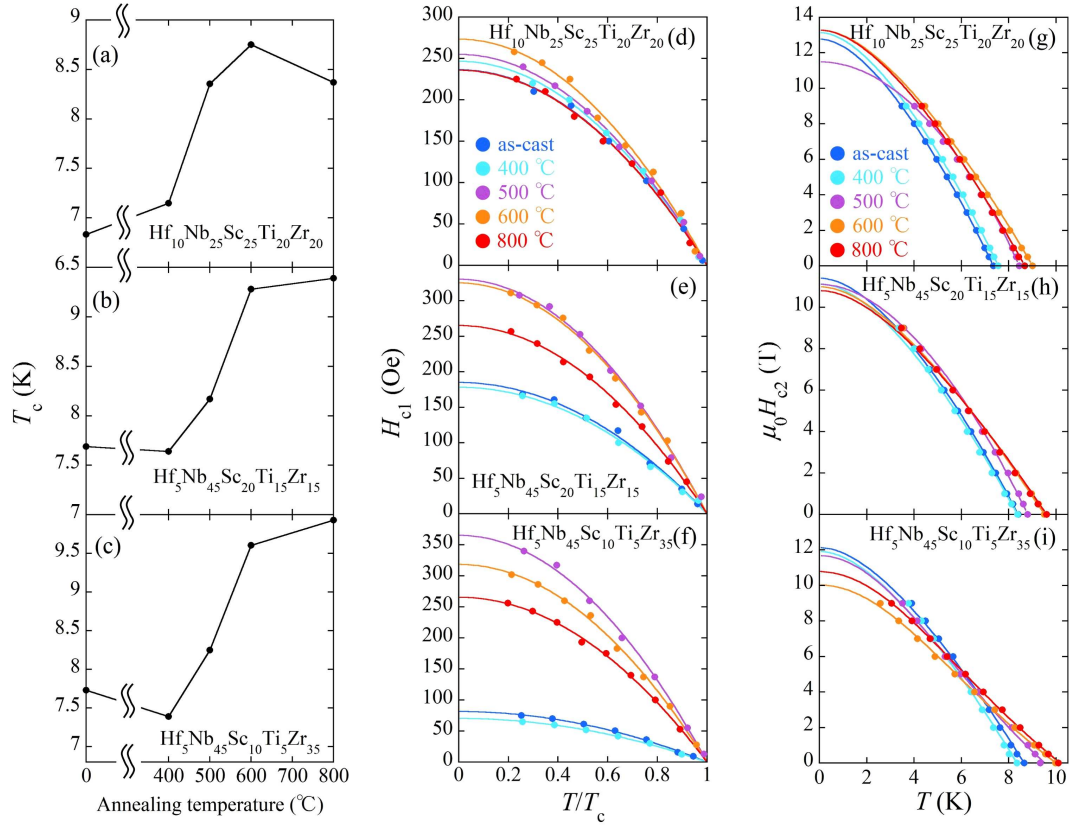


Figure 6: (a)-(c) Annealing temperature dependence of T_c for all alloy systems. T_c is defined as the midpoint of the specific heat jump, except for the as-cast and 400 °C annealed samples of $\text{Hf}_{10}\text{Nb}_{25}\text{Sc}_{25}\text{Ti}_{20}\text{Zr}_{20}$ and the 500 °C annealed sample of $\text{Hf}_5\text{Nb}_{45}\text{Sc}_{10}\text{Ti}_5\text{Zr}_{35}$. For these three samples, T_c is determined using the midpoint of the diamagnetic transition. Temperature dependence of (d)-(f) lower critical field and (g)-(i) upper critical field for all alloy systems. In (d)-(f), the solid curves represent the fitting results using Eq. (1). In (g)-(i), the solid curves correspond to the fitting results using Eq. (2) or $H_{c2}(T) = H_{c2}(0)(1 - (T/T_c)^2)/(1 + (T/T_c)^2)$.

its of 3.52 and 1.43, respectively[14, 34, 35, 36, 37, 38]. Here, $\Delta(0)$ denotes the superconducting gap at zero temperature, k_B is the Boltzmann constant, ΔC_{el} represents the specific heat jump at T_c , and γ is the electronic specific heat coefficient. The electronic specific heat C_{el} is obtained by subtracting the phonon contribution, expressed as βT^3 , from C_p . The γ and β values are determined by fitting $C_p(T)$ in the normal state using the relation $\gamma T + \beta T^3$ (refer to Figs. 5(b), (d), and (f)). The (γ (mJ/mol·K²), β (mJ/mol·K⁴)) values for the as-cast, 400 °C, 500 °C, 600 °C, and 800 °C samples are estimated to be (6.72, 0.153), (6.70, 0.153), (5.40, 0.133), (4.83, 0.132), and (5.10, 0.135) in Hf₁₀Nb₂₅Sc₂₅Ti₂₀Zr₂₀; (6.72, 0.153), (6.70, 0.153), (6.68, 0.132), (6.70, 0.130), and (6.65, 0.128) in Hf₅Nb₄₅Sc₂₀Ti₁₅Zr₁₅; and (7.62, 0.220), (6.51, 0.180), (6.18, 0.142), (5.80, 0.120), and (5.10, 0.132) in Hf₅Nb₄₅Sc₁₀Ti₅Zr₃₅, respectively. For the as-cast and 400 °C annealed samples of Hf₅Nb₄₅Sc₁₀Ti₅Zr₃₅, which consist solely of the bcc phase, the Debye temperature θ_D is estimated from the β value using the relation $\theta_D = \left(\frac{12\pi^4 RN}{5\beta}\right)^{1/3}$, where R is the gas constant and $N = 1$ is the number of atoms per formula unit. The θ_D values are 207 K and 221 K for the as-cast and 400 °C annealed samples, respectively. To evaluate the $\frac{2\Delta(0)}{k_B T_c}$ ratio, C_{el} is calculated within the α -model[39, 40] using the equation:

$$\frac{C_{\text{el}}(t)}{\gamma T_c} = \frac{6\alpha^3}{\pi^2 t} \int_0^\infty f(1-f) \left(\frac{\tilde{E}^2}{t} - \frac{1}{2} \frac{d\tilde{\Delta}^2}{dt} \right) d\tilde{\epsilon}, \quad (4)$$

where $\alpha = \Delta(0)/k_B T_c$ is an adjustable parameter, $\tilde{\epsilon} = \epsilon/\Delta(0)$ is the normalized energy, $\tilde{E} = \sqrt{\tilde{\epsilon}^2 + \tilde{\Delta}^2}$ is the normalized energy of superconducting quasi-particle excitations, f is the Fermi distribution function, and $\tilde{\Delta} = \Delta/\Delta(0)$ is the superconducting gap normalized to its zero-temperature value. The BCS weak-coupling limit corresponds to $\alpha = 1.76$.

In the current analysis, all samples - except the as-cast and 400 °C annealed samples of Hf₅Nb₄₅Sc₁₀Ti₅Zr₃₅ - require an electronic specific heat contribution attributable to the normal state, even within the superconducting regime. Given that the as-cast and 400 °C annealed samples of Hf₅Nb₄₅Sc₁₀Ti₅Zr₃₅ exhibit solely the bcc phase, it is inferred that the hcp phase in the other samples remains in the normal state down to 2 K. Accordingly, the electronic specific heat contribution from the hcp phase is modeled as $\gamma_{\text{hcp}} T$, where γ_{hcp} denotes the hcp contribution to the total γ . Therefore,

the temperature-dependent electronic specific heat $C_{\text{el}}(T)$ is described by:

$$C_{\text{el}}(t) = \frac{\gamma_{\text{bcc}}}{\gamma} C_{\text{el } \alpha\text{-model}}(t) + \frac{\gamma_{\text{hcp}}}{\gamma} T, \quad (5)$$

where γ_{bcc} and $C_{\text{el } \alpha\text{-model}}(t)$ denote the bcc-phase contribution to γ and the electronic specific heat calculated via the α -model, respectively. T_c is defined as the midpoint of the specific heat jump. The discontinuities in C_{el} at T_c are determined by extrapolating data below and above T_c , as shown by dashed lines in Figs. S13-S15 of the Supplementary Material. In computing $\frac{\Delta C_{\text{el}}}{\gamma T_c}$, γ is replaced by γ_{bcc} . It is noted that $\frac{2\Delta(0)}{k_B T_c}$ and $\frac{\Delta C_{\text{el}}}{\gamma T_c}$ are not evaluated for the as-cast and 400 °C annealed samples of $\text{Hf}_{10}\text{Nb}_{25}\text{Sc}_{25}\text{Ti}_{20}\text{Zr}_{20}$ and the 500 °C annealed sample of $\text{Hf}_5\text{Nb}_{45}\text{Sc}_{10}\text{Ti}_5\text{Zr}_{35}$, due to their extremely broad transitions, which hinder accurate parameter extraction.

Figures 7(a)-(l) depict the $C_{\text{el}}/\gamma T$ vs. T/T_c plots for all studied systems. The solid lines represent fits obtained using Eq. (5), and the extracted parameters are summarized in Table 3. The resulting $\frac{2\Delta(0)}{k_B T_c}$ and $\frac{\Delta C_{\text{el}}}{\gamma_{\text{bcc}} T_c}$ values, which both exceed the BCS weak-coupling limits of 3.52 and 1.43, underscore that the Hf-Nb-Sc-Ti-Zr system resides in the strong-coupling regime. As seen in Figs. 7(a)-(c) for the $\text{Hf}_{10}\text{Nb}_{25}\text{Sc}_{25}\text{Ti}_{20}\text{Zr}_{20}$ samples, α values greater than 1.76 are necessary to reproduce the pronounced specific heat jumps. The weak-coupling value of $\alpha = 1.76$ underestimates the jump magnitude, as illustrated by the dashed line in Fig. 7(c). Nonetheless, the overall fitting quality is limited by upper deviations of the experimental data from theoretical predictions, suggesting the presence of additional quasi-particle excitations in the superconducting state. Similarly, the $\text{Hf}_5\text{Nb}_{45}\text{Sc}_{20}\text{Ti}_{15}\text{Zr}_{15}$ system also requires enhanced α values to reproduce $C_{\text{el}}(T)$ (Figs. 7(d)-(h)). For samples annealed below 500 °C, relatively large deviations between experimental and theoretical curves persist below and above T_c , likely due to sample inhomogeneity stemming from insufficient annealing. The as-cast and 400 °C annealed samples of $\text{Hf}_5\text{Nb}_{45}\text{Sc}_{10}\text{Ti}_5\text{Zr}_{35}$, which lack an hcp phase, require no γ_{hcp} contribution. For these samples, the strong-coupling α -model effectively reproduces the experimental data (Figs. 7(i) and (j)). The weak-coupling BCS value of $\alpha = 1.76$ is inadequate to describe the temperature dependence. In the 800 °C annealed sample, a value of α exceeding 1.76 is again necessary. However, minor upper deviations in the experimental data, akin to those in the $\text{Hf}_{10}\text{Nb}_{25}\text{Sc}_{25}\text{Ti}_{20}\text{Zr}_{20}$ samples, are observed (Fig. 7(l)).

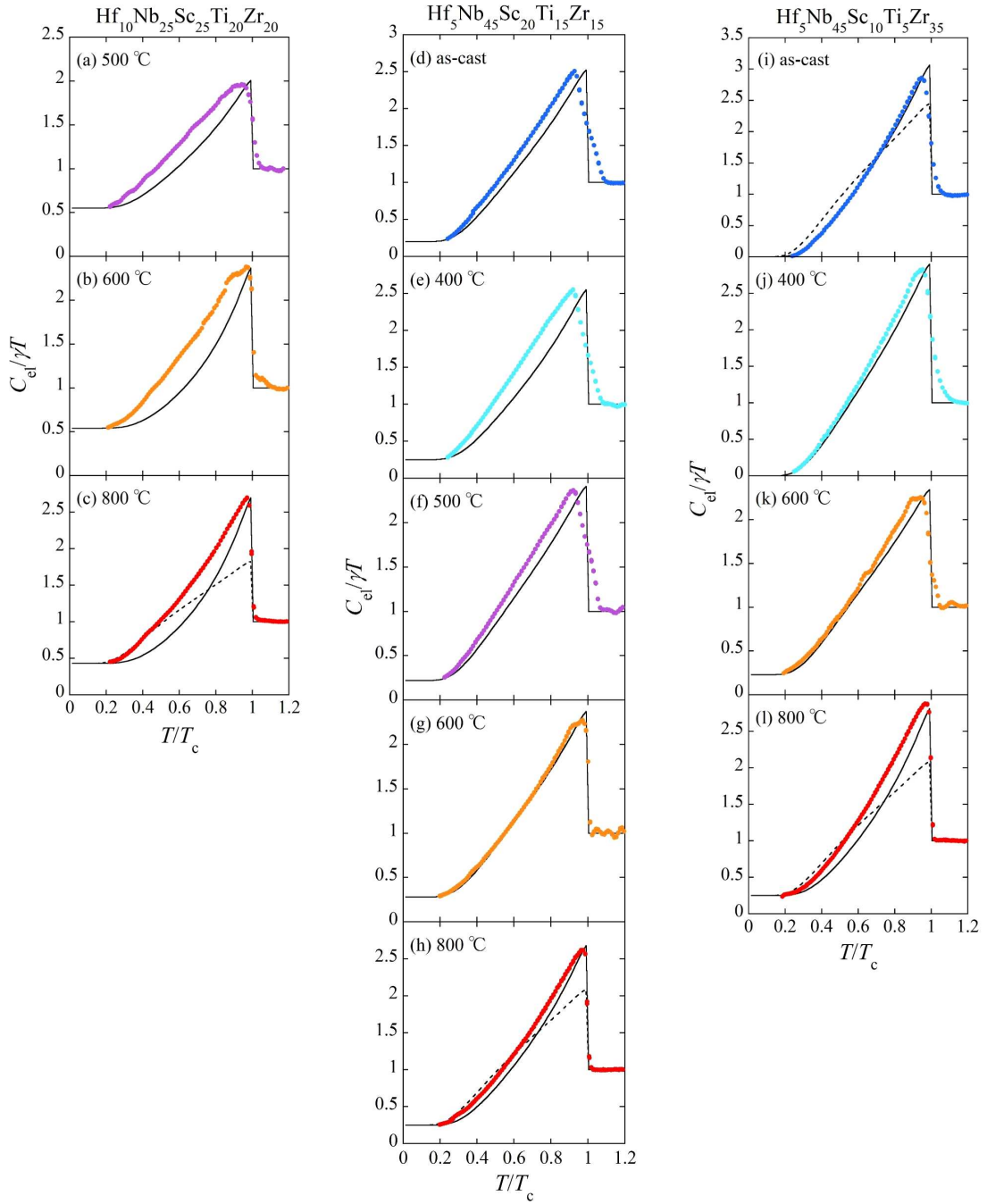


Figure 7: $C_{el}/\gamma T$ vs. T/T_c plots for (a)-(c) $\text{Hf}_{10}\text{Nb}_{25}\text{Sc}_{25}\text{Ti}_{20}\text{Zr}_{20}$, (d)-(h) $\text{Hf}_5\text{Nb}_{45}\text{Sc}_{20}\text{Ti}_{15}\text{Zr}_{15}$, and (i)-(l) $\text{Hf}_5\text{Nb}_{45}\text{Sc}_{10}\text{Ti}_5\text{Zr}_{35}$ systems, respectively. The solid lines represent fitting results using Eq. (5), while the dashed lines correspond to fittings using Eq. (5) with $\alpha=1.76$.

Table 3: α , $\frac{\gamma_{\text{bcc}}}{\gamma}$, $\frac{\gamma_{\text{hcp}}}{\gamma}$, $\frac{2\Delta(0)}{k_{\text{B}}T_c}$, $\frac{\Delta C_{\text{el}}}{\gamma_{\text{bcc}}T_c}$, ω_{ln} , and λ_{ep} of Hf-Nb-Sc-Ti-Zr systems.

sample	α	$\frac{\gamma_{\text{bcc}}}{\gamma}$	$\frac{\gamma_{\text{hcp}}}{\gamma}$	$\frac{2\Delta(0)}{k_{\text{B}}T_c}$	$\frac{\Delta C_{\text{el}}}{\gamma_{\text{bcc}}T_c}$	ω_{ln} (K)	λ_{ep}
Hf ₁₀ Nb ₂₅ Sc ₂₅ Ti ₂₀ Zr ₂₀							
500 °C	2.2	0.45	0.55	4.4	2.19	83.8	1.44
600 °C	2.55	0.46	0.54	5.1	3.07	44.8	4.19
800 °C	2.55	0.57	0.43	5.1	3.13	42.6	4.26
Hf ₅ Nb ₄₅ Sc ₂₀ Ti ₁₅ Zr ₁₅							
as-cast	2.02	0.8	0.2	4.04	2.18	92.5	1.24
400 °C	2.11	0.75	0.25	4.22	2.12	87.2	1.29
500 °C	1.97	0.78	0.22	3.94	1.91	128	1.04
600 °C	2.02	0.72	0.28	4.04	1.8	149	1.03
800 °C	2.2	0.75	0.25	4.4	2.33	87.7	1.54
Hf ₅ Nb ₄₅ Sc ₁₀ Ti ₅ Zr ₃₅							
as-cast	2.11	1.0	0.0	4.22	2.04	92.8	1.24
400 °C	2.02	1.0	0.0	4.04	1.75	124	1.00
600 °C	1.94	0.77	0.23	3.88	1.68	203	0.88
800 °C	2.29	0.75	0.25	4.58	2.68	73.6	2.01

3.3. Critical current density

J_c is calculated using the critical state model, expressed as follows[41]:

$$J_c = \frac{3\Delta M}{\frac{3}{2}a \left(1 - \frac{a}{3b}\right)}, \quad (6)$$

where ΔM is the width of the isothermal M - H hysteresis loop at an applied magnetic field H , and a and b ($b > a$) denote the sample dimensions perpendicular to H . The experimental M - H hysteresis loops at 4.2 and 2 K for all samples are presented in Figs. S16(a)-(f) in the Supplementary Material. Some figures exhibit abrupt changes in magnetization M , more pronounced at the lower temperature of 2 K. This behavior, commonly observed in various superconductors, including other bcc HEAs[22, 29, 42], is attributed to flux jumps, indicative of strong flux pinning. The field-dependent J_c values, determined via the critical state model, are illustrated in Figs. 8(a)-(f). Dashed lines denote the practical threshold of 10^5 A/cm², typically considered the benchmark for superconducting wire applications[22, 43, 44]. For comparison, J_c data of NbScTiZr annealed at 400 °C (solid lines)[19] and

$\text{Ta}_{1/6}\text{Nb}_{2/6}\text{Hf}_{1/6}\text{Zr}_{1/6}\text{Ti}_{1/6}$ annealed at 550 °C (dash-dotted lines)[28] are also shown.

In both $\text{Hf}_{10}\text{Nb}_{25}\text{Sc}_{25}\text{Ti}_{20}\text{Zr}_{20}$ and $\text{Hf}_5\text{Nb}_{45}\text{Sc}_{20}\text{Ti}_{15}\text{Zr}_{15}$ systems, J_c values at 4.2 K and 2 K increase with annealing temperature up to 500 °C across the entire magnetic field range. At each temperature, the samples annealed at 500 °C exhibit superior performance, with J_c surpassing 10^5 A/cm² up to approximately 2.5 T (at 4.2 K) and 4 T (at 2 K) for $\text{Hf}_{10}\text{Nb}_{25}\text{Sc}_{25}\text{Ti}_{20}\text{Zr}_{20}$, and 3 T (at 4.2 K) and 5 T (at 2 K) for $\text{Hf}_5\text{Nb}_{45}\text{Sc}_{20}\text{Ti}_{15}\text{Zr}_{15}$. Heat treatments above 500 °C lead to a systematic degradation of J_c across the examined field range. The annealing temperature dependence of J_c correlates well with the variation in lattice parameter, as shown in Fig. 1(d), which reaches a minimum at ~ 500 °C, signifying enhanced lattice strain. As reported for $\text{Ta}_{1/6}\text{Nb}_{2/6}\text{Hf}_{1/6}\text{Zr}_{1/6}\text{Ti}_{1/6}$ and $(\text{TaNb})_{0.7}(\text{HfZrTi})_{0.5}$, increased lattice strain can enhance J_c via strengthened flux pinning[19, 28, 29]. Notably, the 500 °C annealed $\text{Hf}_{10}\text{Nb}_{25}\text{Sc}_{25}\text{Ti}_{20}\text{Zr}_{20}$ sample partially contains a fine eutectic structure with ~ 80 nm spacing. As previously observed in NbScTiZr, such fine eutectic structures serve as effective flux pinning centers[25, 26]. However, in $\text{Hf}_{10}\text{Nb}_{25}\text{Sc}_{25}\text{Ti}_{20}\text{Zr}_{20}$, this structure does not uniformly permeate the sample, likely limiting the flux pinning effect, reflected in the relatively lower J_c compared to NbScTiZr, as seen in Figs. 8(a) and (b). The J_c values of the 500 °C samples in both $\text{Hf}_{10}\text{Nb}_{25}\text{Sc}_{25}\text{Ti}_{20}\text{Zr}_{20}$ and $\text{Hf}_5\text{Nb}_{45}\text{Sc}_{20}\text{Ti}_{15}\text{Zr}_{15}$ are comparable to those reported for $\text{Ta}_{1/6}\text{Nb}_{2/6}\text{Hf}_{1/6}\text{Zr}_{1/6}\text{Ti}_{1/6}$ annealed at 550 °C[28], reinforcing the pivotal role of lattice strain in flux pinning.

The as-cast $\text{Hf}_5\text{Nb}_{45}\text{Sc}_{10}\text{Ti}_5\text{Zr}_{35}$ sample, lacking eutectic structure and exhibiting minimal lattice strain as suggested by Fig. 1(d), displays markedly lower J_c (Figs. 8(e) and (f)) in comparison to the other two systems. Although the 400 °C annealed sample also exhibits reduced J_c , a fishtail effect is observed at higher magnetic fields. The enhancement in J_c at elevated fields likely underpins the significantly improved J_c across the entire magnetic field range for the 500 °C annealed sample, which lies near a phase instability, as discussed in the $C_p(T)$ results. Remarkably, the J_c of the 500 °C annealed $\text{Hf}_5\text{Nb}_{45}\text{Sc}_{10}\text{Ti}_5\text{Zr}_{35}$ sample exceeds 10^5 A/cm² up to nearly 4 T (at 4.2 K) and 6 T (at 2 K), classifying it among the highest-performing HEAs in terms of J_c . Similar to the other systems, further annealing at higher temperatures diminishes J_c , and the annealing temperature dependence of the lattice parameter suggests that increased lattice strain contributes to the enhanced flux pinning observed at 500 °C. Although SEM analysis of this sample reveals a partially developed fine eutectic structure with ~ 40 nm

spacing, its contribution to flux pinning may be limited, akin to the case of $\text{Hf}_{10}\text{Nb}_{25}\text{Sc}_{25}\text{Ti}_{20}\text{Zr}_{20}$. This may explain the relatively lower J_c at low magnetic fields in the 500 °C annealed $\text{Hf}_5\text{Nb}_{45}\text{Sc}_{10}\text{Ti}_5\text{Zr}_{35}$ sample compared to NbScTiZr (Figs. 8(e) and (f)). Nevertheless, at higher fields ($1 \text{ T} < \mu_0 H < 4.5 \text{ T}$ at 4.2 K and $\mu_0 H > 1.5 \text{ T}$ at 2 K), the J_c of the 500 °C annealed sample surpasses those of both $\text{Ta}_{1/6}\text{Nb}_{2/6}\text{Hf}_{1/6}\text{Zr}_{1/6}\text{Ti}_{1/6}$ and NbScTiZr, suggesting an additional flux pinning mechanism beyond lattice strain. As previously noted, the specific heat displays an exceptionally broad anomaly following 500 °C annealing in $\text{Hf}_5\text{Nb}_{45}\text{Sc}_{10}\text{Ti}_5\text{Zr}_{35}$, implying a phase instability that could plausibly serve as an additional flux pinning source.

To elucidate the flux pinning mechanism, the flux pinning force density (F_p) was calculated using the relation $F_p = \left| \mu_0 \vec{H} \times \vec{J}_c \right|$. Subsequently, the normalized flux pinning force density, $f_p (= F_p / F_{p \text{ max}})$, was evaluated as a function of H / H_{peak} , where $F_{p \text{ max}}$ and H_{peak} represent the maximum value of F_p and the corresponding magnetic field, respectively. The experimental data were compared with representative theoretical models:

$$f_p = \frac{25}{16} \left(\frac{H}{H_{\text{peak}}} \right)^{0.5} \left(1 - \frac{1}{5} \frac{H}{H_{\text{peak}}} \right)^2 \quad (7)$$

for normal surface pinning and

$$f_p = \frac{9}{4} \left(\frac{H}{H_{\text{peak}}} \right) \left(1 - \frac{1}{3} \frac{H}{H_{\text{peak}}} \right)^2 \quad (8)$$

for normal point pinning[45, 46, 47]. Figures 9(a)-(o) present f_p as a function of H / H_{peak} for all systems at 2 and 4.2 K, overlaid with theoretical curves corresponding to the surface and point pinning mechanisms.

In the $\text{Hf}_{10}\text{Nb}_{25}\text{Sc}_{25}\text{Ti}_{20}\text{Zr}_{20}$ system, the as-cast sample follows the surface pinning model, suggesting that grain boundaries between the bcc and hcp phases serve as primary flux pinning sites (Fig. 9(a)). The samples annealed at 500 °C and 600 °C exhibit significant deviations from both models at higher magnetic fields, although their low-field behavior aligns with the point pinning mechanism (Figs. 9(c) and (d)). Notably, the 600 °C annealed sample displays a shoulder-like feature centered around $H / H_{\text{peak}} = 1$, indicating the coexistence of multiple pinning mechanisms. While this shoulder structure persists in the 800 °C annealed sample, the surface pinning model again describes the experimental data (Fig. 9(e)). The predominant pinning mechanism in $\text{Ta}_{1/6}\text{Nb}_{2/6}\text{Hf}_{1/6}\text{Zr}_{1/6}\text{Ti}_{1/6}$ annealed at 550 °C is known

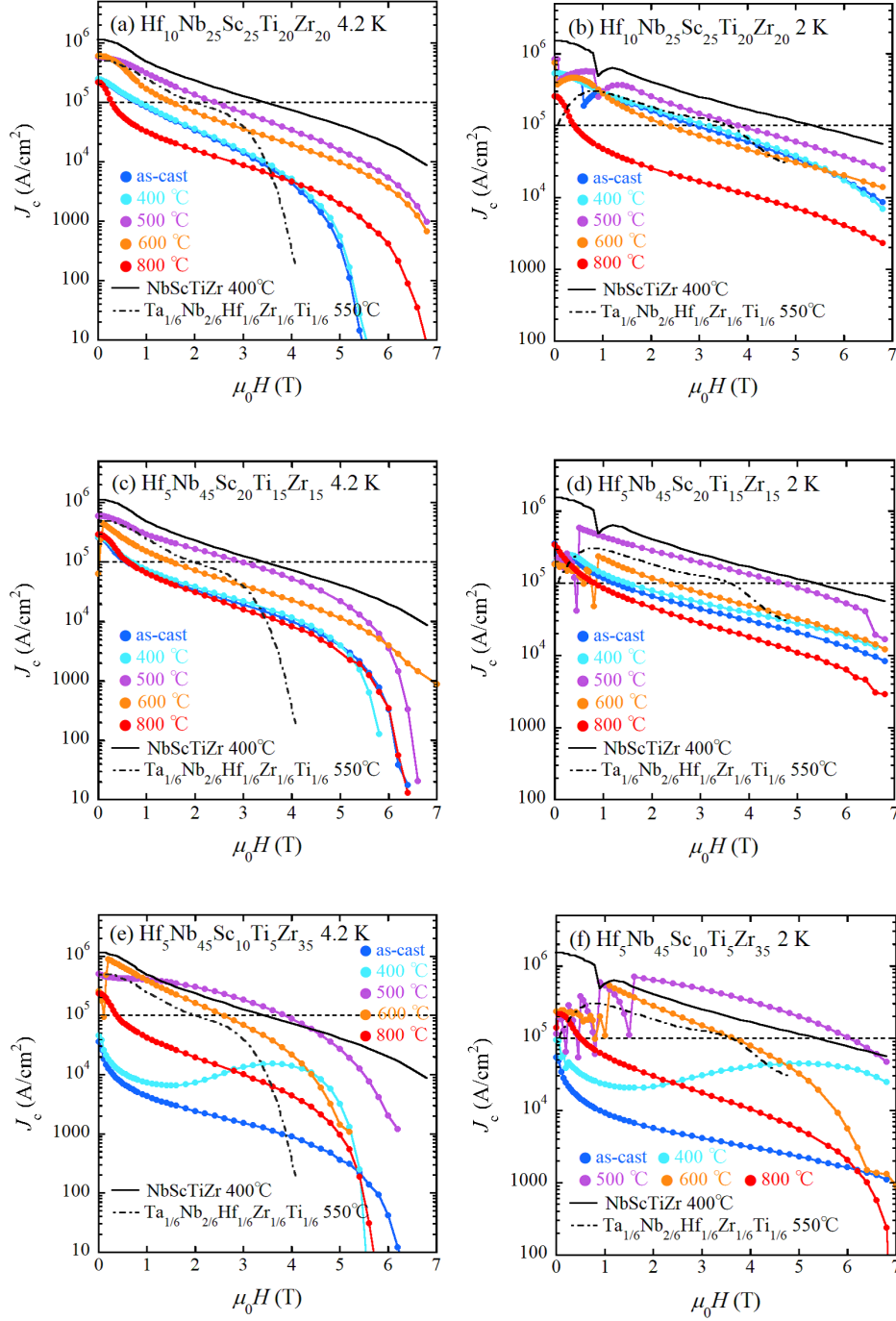


Figure 8: (a) and (b) Magnetic field dependence of J_c for $\text{Hf}_{10}\text{Nb}_{25}\text{Sc}_{25}\text{Ti}_{20}\text{Zr}_{20}$ at 4.2 and 2 K, respectively. (c) and (d) Magnetic field dependence of J_c for $\text{Hf}_5\text{Nb}_{45}\text{Sc}_{20}\text{Ti}_{15}\text{Zr}_{15}$ at 4.2 and 2 K, respectively. (e) and (f) Magnetic field dependence of J_c for $\text{Hf}_5\text{Nb}_{45}\text{Sc}_{10}\text{Ti}_5\text{Zr}_{35}$ at 4.2 and 2 K, respectively. The dashed lines indicate the practical benchmark level for superconducting wire applications. The solid and dash-dotted lines represent J_c values of NbScTiZr annealed at 400 °C[19] and $\text{Ta}_{1/6}\text{Nb}_{2/6}\text{Hf}_{1/6}\text{Zr}_{1/6}\text{Ti}_{1/6}$ annealed at 550 °C[28], respectively.

to be normal point pinning[28]. In contrast, NbScTiZr annealed at 400 °C demonstrates considerable deviations from both the point and surface pinning models[19]. In the 500 °C annealed $\text{Hf}_{10}\text{Nb}_{25}\text{Sc}_{25}\text{Ti}_{20}\text{Zr}_{20}$ sample, the pinning force at low fields is primarily governed by the point pinning mechanism, consistent with the low-field J_c behavior (Figs. 8(a) and (b)) resembling that of $\text{Ta}_{1/6}\text{Nb}_{2/6}\text{Hf}_{1/6}\text{Zr}_{1/6}\text{Ti}_{1/6}$ [28]. As illustrated in Figs. 9(f)-(j), the normal surface pinning model predominantly accounts for the pinning behavior in most $\text{Hf}_5\text{Nb}_{45}\text{Sc}_{20}\text{Ti}_{15}\text{Zr}_{15}$ samples. The exception is the 500 °C annealed sample, whose experimental data lie between the surface and point pinning models. This suggests that lattice strain, considered a point pinning source, partially contributes to the pinning mechanism. For the as-cast $\text{Hf}_5\text{Nb}_{45}\text{Sc}_{10}\text{Ti}_5\text{Zr}_{35}$ sample, a single pinning model fails to describe the data; instead, the surface pinning model agrees with low-field behavior, while the point pinning model captures the high-field response (Fig. 9(k)). Neither model sufficiently explains the fishtail effect observed in the 400 °C annealed sample (Fig. 9(l)). The experimental plots of the 500 °C and 800 °C annealed samples correspond well with the theoretical curves for point and surface pinning mechanisms, respectively (Figs. 9(m) and (o)). Although the 600 °C annealed sample largely follows the surface pinning model, its low-field data do not substantially deviate from the point pinning model.

The pinning force analysis reveals that the normal point pinning mechanism is dominant over the surface pinning mechanism, particularly in the 500 °C annealed samples of $\text{Hf}_{10}\text{Nb}_{25}\text{Sc}_{25}\text{Ti}_{20}\text{Zr}_{20}$ and $\text{Hf}_5\text{Nb}_{45}\text{Sc}_{10}\text{Ti}_5\text{Zr}_{35}$. These samples exhibit increased lattice strain, as indicated by the reduced lattice parameters, similar to the 550 °C annealed $\text{Ta}_{1/6}\text{Nb}_{2/6}\text{Hf}_{1/6}\text{Zr}_{1/6}\text{Ti}_{1/6}$, which also follows the point pinning mechanism. Furthermore, in the 500 °C annealed $\text{Hf}_5\text{Nb}_{45}\text{Sc}_{10}\text{Ti}_5\text{Zr}_{35}$ sample, the phase instability, as evidenced by specific heat anomaly, may also contribute to the point pinning behavior.

3.4. Enhanced T_c in Hf-Nb-Sc-Ti-Zr

Figure 10(a) presents the plots of T_c vs. VEC for the investigated Hf-Nb-Sc-Ti-Zr HEAs. T_c corresponds to the midpoint of the superconducting transition observed in $C_p(T)$. The data for the as-cast and 400 °C annealed samples of $\text{Hf}_{10}\text{Nb}_{25}\text{Sc}_{25}\text{Ti}_{20}\text{Zr}_{20}$, as well as the 500 °C annealed sample of $\text{Hf}_5\text{Nb}_{45}\text{Sc}_{10}\text{Ti}_5\text{Zr}_{35}$, were excluded due to their extremely broad superconducting transitions. Error bars are included for the as-cast, 400 °C annealed, and 600 °C annealed samples of $\text{Hf}_5\text{Nb}_{45}\text{Sc}_{10}\text{Ti}_5\text{Zr}_{35}$, since both phase-separated bcc phases exhibit superconductivity in the as-cast and 400

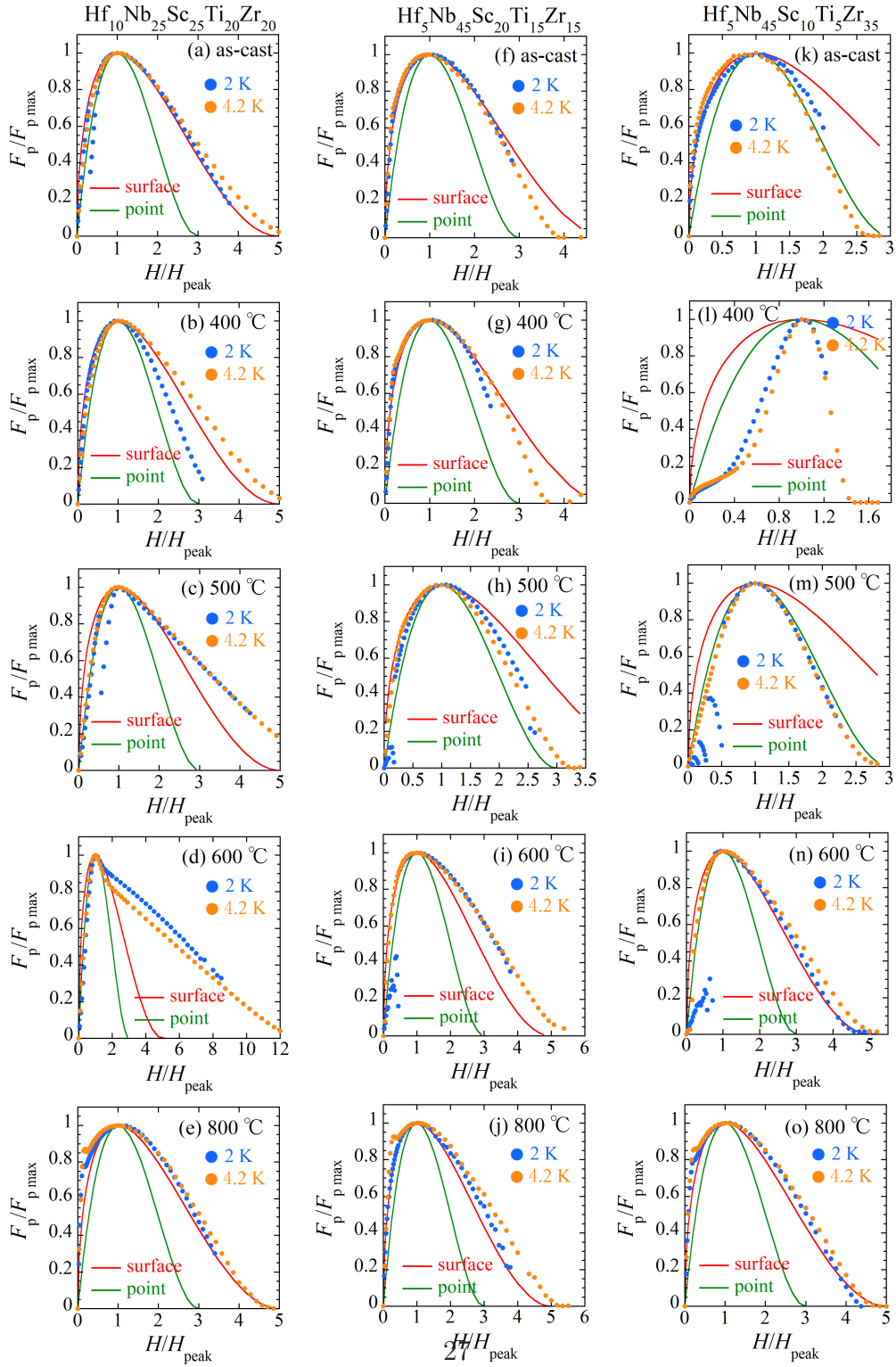


Figure 9: Normalized flux pinning force densities as a function of H/H_{peak} for (a)-(e) $Hf_{10}Nb_{25}Sc_{25}Ti_{20}Zr_{20}$, (f)-(j) $Hf_5Nb_{45}Sc_{20}Ti_{15}Zr_{15}$, and (k)-(o) $Hf_5Nb_{45}Sc_{10}Ti_5Zr_{35}$, respectively.

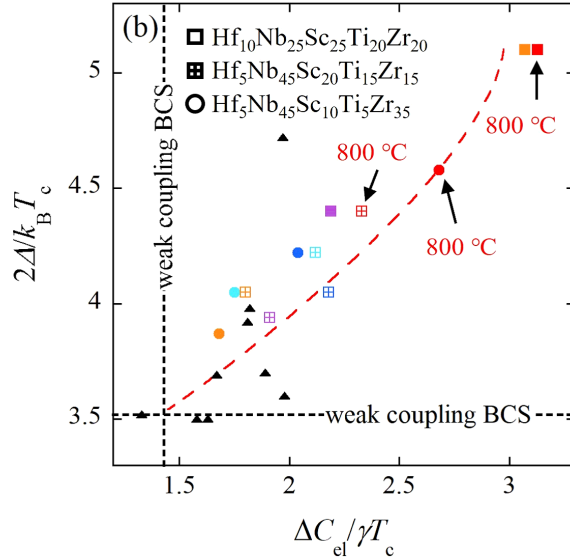
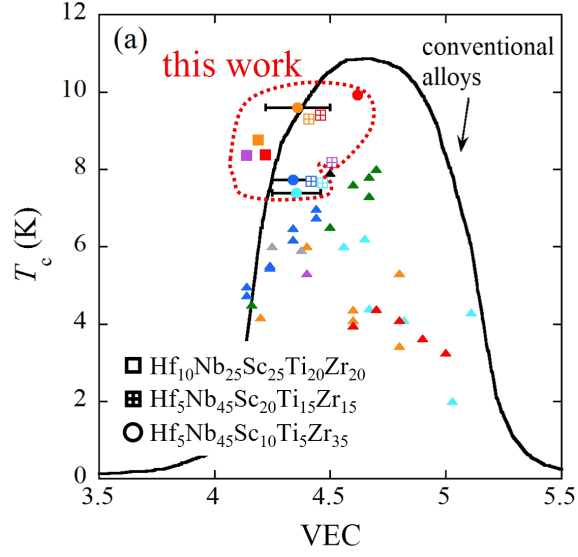


Figure 10: (a) VEC dependence of T_c for Hf-Nb-Sc-Ti-Zr HEAs. Within each Hf-Nb-Sc-Ti-Zr system, blue, light blue, purple, orange, and red represent the as-cast, 400 °C, 500 °C, 600 °C, and 800 °C samples, respectively. Data for typical quinary bcc HEA superconductors are also depicted by filled color triangles. The color correspondence for typical bcc HEAs is as follows: green-non-equimolar Hf-Nb-Ta-Ti-Zr[36]; black-Ta_{1/6}Nb_{2/6}Hf_{1/6}Zr_{1/6}Ti_{1/6}[35]; blue-Al-Nb-Ti-V-Zr[49]; purple-Hf₂₁Nb₂₅Ti₁₅V₁₅Zr₂₄[48]; orange-HfNbTaTiZr, HfNbReTiZr, HfNbTaTiV, HfMoNbTiZr, TiHfNbTaMo, and ScVTiHfNb[32, 34, 37, 38, 50, 51]; light blue-Nb-Ta-Mo-Hf-W, Ti-Zr-Nb-Ta-W, and Ti-Zr-Nb-Ta-V[52, 53]; red-Ti-Hf-Nb-Ta-Re[24]; and grey-Ti_{0.5}(ZrNbHfTa)_{0.5} and Ti_{0.5}(VNbHfTa)_{0.5}[33]. The solid line represents the Matthias rule of conventional binary or ternary transition metal alloys. (b) Correlation between $\frac{2\Delta(0)}{k_B T_c}$ and $\frac{\Delta C_{el}}{\gamma T_c}$ for Hf-Nb-Sc-Ti-Zr and several quinary HEAs. The red dashed line denotes the theoretical prediction calculated using Eqs. (9) and (10).

°C annealed states and the chemical composition of the bcc phase in the eutectic structure cannot be accurately determined for the 600 °C annealed sample. The plot also includes data for typical quinary HEAs, represented by colored triangles. Green, black, blue, and purple triangles indicate non-equimolar Hf-Nb-Ta-Ti-Zr, $\text{Ta}_{1/6}\text{Nb}_{2/6}\text{Hf}_{1/6}\text{Zr}_{1/6}\text{Ti}_{1/6}$, Al-Nb-Ti-V-Zr, and $\text{Hf}_{21}\text{Nb}_{25}\text{Ti}_{15}\text{V}_{15}\text{Zr}_{24}$, respectively[35, 36, 48, 49]. Orange triangles represent data for HfNbTaTiZr, HfNbReTiZr, HfNbTaTiV, HfMoNbTiZr, HfMoNbTaTi, and ScVTiHfNb[32, 34, 37, 38, 50, 51]. Additional systems are indicated by light blue (Nb-Ta-Mo-Hf-W, Ti-Zr-Nb-Ta-W, and Ti-Zr-Nb-Ta-V), red (Ti-Hf-Nb-Ta-Re), and grey ($\text{Ti}_{0.5}(\text{ZrNbHfTa})_{0.5}$ and $\text{Ti}_{0.5}(\text{VNbHfTa})_{0.5}$) triangles[24, 33, 52, 53]. The solid curve represents the Matthias rule for conventional binary or ternary transition-metal alloys. Notably, at a given VEC, most Hf-Nb-Sc-Ti-Zr samples exhibit T_c values higher than those of typical quinary HEAs. It is worth noting that the T_c of $\text{Ta}_{1/6}\text{Nb}_{2/6}\text{Hf}_{1/6}\text{Zr}_{1/6}\text{Ti}_{1/6}$ is comparable to that of Hf-Nb-Sc-Ti-Zr samples with no eutectic structure (i.e., the as-cast and 400 °C annealed $\text{Hf}_5\text{Nb}_{45}\text{Sc}_{10}\text{Ti}_5\text{Zr}_{35}$) or a partial eutectic region (as observed in the as-cast, 400 °C, and 500 °C annealed $\text{Hf}_5\text{Nb}_{45}\text{Sc}_{20}\text{Ti}_{15}\text{Zr}_{15}$). According to BCS theory, T_c depends on γ and θ_D . For instance, the γ and θ_D values of as-cast $\text{Hf}_5\text{Nb}_{45}\text{Sc}_{10}\text{Ti}_5\text{Zr}_{35}$ are 7.62 mJ/mol·K² and 207 K, respectively—comparable to 7.42 mJ/mol·K² and 194 K in $\text{Ta}_{1/6}\text{Nb}_{2/6}\text{Hf}_{1/6}\text{Zr}_{1/6}\text{Ti}_{1/6}$ [35]. This similarity further supports the comparable T_c between these two systems. In each Hf-Nb-Sc-Ti-Zr alloy, higher annealing temperatures lead to an expansion of the eutectic region, eventually encompassing the entire sample, enhancing T_c , and establishing another trend in the T_c -VEC relationship.

To further investigate the underlying factors contributing to the enhanced T_c in Hf-Nb-Sc-Ti-Zr alloys, the relationship between $\frac{2\Delta(0)}{k_B T_c}$ and $\frac{\Delta C_{el}}{\gamma T_c}$ was examined for both Hf-Nb-Sc-Ti-Zr systems and selected quinary HEAs, as depicted in Fig. 10(b). These ratios are not shown for the as-cast and 400 °C annealed $\text{Hf}_{10}\text{Nb}_{25}\text{Sc}_{25}\text{Ti}_{20}\text{Zr}_{20}$ samples and the 500 °C annealed $\text{Hf}_5\text{Nb}_{45}\text{Sc}_{10}\text{Ti}_5\text{Zr}_{35}$ sample due to their broad C_p transitions, from which reliable parameters could not be extracted. The primary superconducting parameters of selected quinary HEAs are summarized in Table 4. Many HEAs fall within the strong-coupling regime, implying that strong coupling might be an intrinsic feature of bcc-structured HEAs. The parameters $\frac{2\Delta(0)}{k_B T_c}$ and $\frac{\Delta C_{el}}{\gamma T_c}$ in the strong-coupling limit are given by the following expressions[54,

Table 4: T_c , VEC, $\frac{2\Delta(0)}{k_B T_c}$, and $\frac{\Delta C_{el}}{\gamma T_c}$ of typical quinary HEAs.

HEA	T_c (K)	VEC	$\frac{2\Delta(0)}{k_B T_c}$	$\frac{\Delta C_{el}}{\gamma T_c}$	reference
Ta ₃₄ Nb ₃₃ Hf ₈ Zr ₁₄ Ti ₁₁	7.3	4.67	3.5	1.63	[14]
(Ta ₁ Nb) _{0.67} (ZrHfTi) _{0.33}	7.8	4.67	3.7	1.89	[36]
(Ta ₁ Nb) _{0.16} (ZrHfTi) _{0.84}	4.5	4.16	3.6	1.98	[36]
Ta _{1/6} Nb _{2/6} Hf _{1/6} Zr _{1/6} Ti _{1/6}	7.9	4.5	4.72	1.97	[35]
HfNbTaTiV	5.0	4.6	3.69	1.67	[37]
HfNbReTiZr	5.3	4.8	3.92	1.81	[34]
HfMoNbTiZr	4.1	4.6	3.5	1.58	[50]
HfMoNbTaTi	3.42	4.8	3.98	1.82	[38]
HfNbScTiV	4.17	4.2	3.52	1.33	[32]

55]:

$$\frac{2\Delta(0)}{k_B T_c} = 3.53 \left[1 + 12.5 \left(\frac{k_B T_c}{\omega_{ln}} \right)^2 \ln \left(\frac{\omega_{ln}}{2k_B T_c} \right) \right] \quad (9)$$

$$\frac{\Delta C_{el}}{\gamma T_c} = 1.43 \left[1 + 53 \left(\frac{k_B T_c}{\omega_{ln}} \right)^2 \ln \left(\frac{\omega_{ln}}{3k_B T_c} \right) \right], \quad (10)$$

where ω_{ln} is the logarithmic average of phonon frequencies. The red dashed line in Fig. 10(b) represents the theoretical relationship derived from these equations. The data points for Hf-Nb-Sc-Ti-Zr alloys align with this line, confirming that these systems are indeed strong-coupled superconductors. Most Hf-Nb-Sc-Ti-Zr samples annealed at lower temperatures exhibit slightly stronger coupling than other quinary HEA systems except Ta_{1/6}Nb_{2/6}Hf_{1/6}Zr_{1/6}Ti_{1/6}. This observation suggests that the specific elemental combination in Hf-Nb-Sc-Ti-Zr alloys contributes to the slightly elevated T_c values. Higher annealing temperatures in Hf-Nb-Sc-Ti-Zr alloys promote the development of a fully eutectic microstructure, most prominently observed in the 800 °C annealed samples across all compositions. Figure 10(b) indicates that these 800 °C annealed samples shift the $\frac{2\Delta(0)}{k_B T_c}$ vs. $\frac{\Delta C_{el}}{\gamma T_c}$ relationship toward a stronger coupling regime, which correlates with the observed enhancement in T_c . These analyses underscore the pivotal role of eutectic structures in enhancing superconducting transition temperature.

Here, we examine the mechanism underlying strong-coupling superconductivity in Hf-Nb-Sc-Ti-Zr alloys. Using Eqs. (9) and (10), the ω_{ln} value of

each sample was extracted, as summarized in Table 3. The degree of strong coupling was evaluated through the electron–phonon coupling constant λ_{ep} , obtained from the McMillan equation modified by Allen and Dynes[56], expressed as

$$T_c = \frac{\omega_{\text{ln}}}{1.20} \exp \left(-1.04 \frac{1 + \lambda_{\text{ep}}}{\lambda_{\text{ep}} - \mu^*(1 + 0.62\lambda_{\text{ep}})} \right). \quad (11)$$

Assuming a constant Coulomb pseudopotential $\mu^*=0.13$, a value widely adopted for many transition-metal-based superconductors[57], λ_{ep} was calculated by substituting T_c , ω_{ln} , and μ^* into Eq. (11). The resulting λ_{ep} values are listed in Table 3. Niobium is known as a strong-coupling superconductor with $\lambda_{\text{ep}} \sim 1.0$ [58], which is comparable to those of $\text{Hf}_5\text{Nb}_{45}\text{Sc}_{20}\text{Ti}_{15}\text{Zr}_{15}$ and $\text{Hf}_5\text{Nb}_{45}\text{Sc}_{10}\text{Ti}_5\text{Zr}_{35}$ at lower annealing temperatures. This indicates that the strong-coupling strength of Nb-rich HEAs mirrors that of elemental Nb. The annealing-temperature dependence of λ_{ep} in $\text{Hf}_5\text{Nb}_{45}\text{Sc}_{20}\text{Ti}_{15}\text{Zr}_{15}$ and $\text{Hf}_5\text{Nb}_{45}\text{Sc}_{10}\text{Ti}_5\text{Zr}_{35}$ reveals that λ_{ep} decreases temporarily at intermediate temperatures (500-600 °C) but increases again at higher temperatures. Notably, the decrease in λ_{ep} within the 500-600 °C range is attributed to the enhanced ω_{ln} , suggesting phonon hardening. In these alloys annealed at 500-600 °C, fine microstructures comprising bcc and hcp phases emerge. The interfaces between these phases act as barriers to dislocation motion due to the mismatch of mechanical and structural properties, thereby inducing high hardness[59, 60]. Such interface strengthening is consistent with the pronounced lattice strain observed in Fig. 1(d) and likely contributes to phonon hardening, thereby explaining the enhanced ω_{ln} . In contrast, coarsened microstructures in high-temperature-annealed samples of all systems, including $\text{Hf}_{10}\text{Nb}_{25}\text{Sc}_{25}\text{Ti}_{20}\text{Zr}_{20}$, exhibit reduced interfacial areas, which relax interface strengthening and consequently lead to phonon softening. Therefore, Hf-Nb-Sc-Ti-Zr alloys subjected to high-temperature annealing tend to exhibit decreased ω_{ln} , thereby promoting an enhanced λ_{ep} . We note that NbScTiZr displays a reduction in hardness upon high-temperature annealing[26], corroborating that coarsened microstructures induce phonon softening. L. Zeng et al. systematically compiled the superconducting parameters of transition-metal-based superconductors in the strong-coupling regime[58]. According to their analysis, phonon softening plays a pivotal role in enhancing λ_{ep} . This is consistent with the McMillan formalism, in which λ_{ep} is defined as $\lambda_{\text{ep}} = \frac{N(E_F)\langle I^2 \rangle}{M_w\langle \omega^2 \rangle}$, where $N(E_F)$ is the density of states at the Fermi level, M_w is the molecular weight, and $\langle I^2 \rangle$ and $\langle \omega^2 \rangle$ represent the averaged square of

electron-phonon matrix element and the phonon frequency, respectively[57]. In this framework, phonon softening corresponds to a reduction in $\langle\omega^2\rangle$, which enhances λ_{ep} . We therefore infer that significant lattice strain is detrimental to strong-coupling superconductivity, whereas pronounced phonon softening, facilitated by the relaxation of interface strengthening during high-temperature annealing, ensures the manifestation of strong-coupling superconductivity in Hf-Nb-Sc-Ti-Zr alloys.

4. Summary

We have investigated the superconducting properties of Hf-Nb-Sc-Ti-Zr quinary eutectic HEAs subjected to heat treatments up to 800 °C, aiming to examine the universality of the deviation in the T_c vs. VEC relationship from the trend observed in typical quinary bcc HEAs. Additionally, we explored the correlation between microstructure and J_c . The nominal compositions—Hf₁₀Nb₂₅Sc₂₅Ti₂₀Zr₂₀, Hf₅Nb₄₅Sc₂₀Ti₁₅Zr₁₅, and Hf₅Nb₄₅Sc₁₀Ti₅Zr₃₅—span a broad range of VEC values associated with the bcc phase. The XRD patterns revealed a reduction in lattice parameters of the bcc phases upon annealing at 500-600 °C across all systems, indicative of significant lattice strain. In Hf₁₀Nb₂₅Sc₂₅Ti₂₀Zr₂₀ and Hf₅Nb₄₅Sc₂₀Ti₁₅Zr₁₅, samples annealed at lower temperatures exhibit partial eutectic regions, whereas annealing above 600 °C leads to an expanded eutectic region encompassing the entire sample. Conversely, the as-cast and 400 °C annealed Hf₅Nb₄₅Sc₁₀Ti₅Zr₃₅ samples consist solely of bcc phases, transforming into eutectic structures comprising bcc and hcp phases with increasing annealing temperature. In all systems, T_c increases sharply from the 400 °C to the 600 °C annealed states, reaching a maximum of 9.93 K in the 800 °C annealed Hf₅Nb₄₅Sc₁₀Ti₅Zr₃₅ sample. Specific heat analyses reveal that nearly all samples exhibit characteristics of strong-coupled superconductors. The Hf₅Nb₄₅Sc₁₀Ti₅Zr₃₅ sample annealed at 500 °C demonstrates J_c exceeding the practical threshold of 10⁵ A/cm², sustaining this level up to approximately 4 T at 4.2 K and 6 T at 2 K, indicating that this sample belongs to the highest-performing class of HEAs in terms of J_c . The pronounced lattice strain and inherent phase instability likely contribute to the elevated J_c . Compared to representative quinary bcc HEAs, the T_c versus VEC plot for the Hf-Nb-Sc-Ti-Zr system underscores the enhanced T_c and delineates a distinct VEC dependence that deviates from typical bcc HEA trends. The relationship between $\frac{2\Delta(0)}{k_B T_c}$ and $\frac{\Delta C_{\text{el}}}{\gamma T_c}$ was evaluated to elucidate this result. The Hf-Nb-Sc-Ti-Zr samples reside in the

strong-coupling regime relative to other quinary bcc HEAs. The expansion of the eutectic region in these samples further shifts this relationship toward the stronger-coupling domain, suggesting that the eutectic structure plays a pivotal role in enhancing T_c .

CRedit authorship contribution statement

Issei Kubo: Investigation. Yuto Watanabe: Investigation, Writing - reviewing & editing. Shuma Kawashima: Investigation. Tomohiro Miyaji: Investigation. Yoshikazu Mizuguchi: Investigation, Formal analysis, Writing - reviewing & editing. Terukazu Nishizaki: Investigation, Formal analysis, Writing - reviewing & editing. Jiro Kitagawa: Supervision, Formal analysis, Writing - original draft, Writing - reviewing & editing.

Acknowledgments

J.K. is grateful for the support provided by the Comprehensive Research Organization of Fukuoka Institute of Technology and a Grant-in-Aid for Scientific Research (KAKENHI) (Grant No. 23K04570). Y.M. acknowledges the support from a Grant-in-Aid for Scientific Research (KAKENHI) (Grant No. 21H00151) and JST-ERATO(Grant No. JPMJER2201). T.N. acknowledges the support from a Grant-in-Aid for Scientific Research (KAKENHI) (Grant No. 24K08236) and the Takahashi Industrial and Economic Research Foundation.

Declaration of Competing Interest

The authors have no conflicts to disclose.

Data Availability Statement

The data that support the findings of this study are available on reasonable request.

References

- [1] B. Cantor, I.T.H. Chang, P. Knight, A.J.B. Vincent, Microstructural development in equiatomic multicomponent alloys, *Mater. Sci. Eng. A* 375-377 (2004) 213-218.

- [2] J.-W. Yeh, S.-K. Chen, S.-J. Lin, J.-Y. Gan, T.-S. Chin, T.-T. Shun, C.-H. Tsau, S.-Y. Chang, Nanostructured High-Entropy Alloys with Multiple Principal Elements: Novel Alloy Design Concepts and Outcomes, *Adv. Eng. Mater.* 6 (2004) 299-303.
- [3] M.C. Gao, J.-W. Yeh, P.K. Liaw, Y. Zhang, *High-Entropy Alloys: Fundamentals and Applications*, Springer, Switzerland, (2015).
- [4] B. Cantor, *Fundamentals of Multicomponent High-Entropy Materials*, Oxford University Press, United Kingdom, 2024.
- [5] X. Yan, P.K. Liaw, Y. Zhang, Order and Disorder in Amorphous and High-Entropy, *Materials Metall. Mater. Trans. A* 52, (2021) 2021-2111.
- [6] W. Li, D. Xie, D. Li, Y. Zhang, Y. Gao, P.K. Liaw, Mechanical behavior of high-entropy alloys, *Prog. Mater. Sci.* 118 (2021) 100777.
- [7] Y. Fu, J. Li, H. Luo, C. Du, X. Li, Recent advances on environmental corrosion behavior and mechanism of high-entropy alloys, *J. Mater. Sci. Technol.* 80 (2021) 217-233.
- [8] J. Li, Y. Huang, X. Meng, Y. Xie, A Review on High Entropy Alloys Coatings: Fabrication Processes and Property Assessment, *Adv. Eng. Mater.* 21 (2019) 1900343.
- [9] V. Chaudhary, R. Chaudhary, R. Banerjee, R.V. Ramanujan, Accelerated and conventional development of magnetic high entropy alloys, *Mater. Today* 49 (2021) 231-252.
- [10] J. Kitagawa, Magnetic properties, electrical resistivity, and hardness of high-entropy alloys FeCoNiPd and FeCoNiPt, *J. Magn. Magn. Mater.* 563 (2022) 170024.
- [11] L. Han, S. Zhu, Z. Rao, C. Scheu, D. Ponge, A. Ludwig, H. Zhang, O. Gutfleisch, H. Hahn, Z. Li, D. Raabe, Multifunctional high-entropy materials, *Nat. Rev. Mater.* 9 (2024) 846-865.
- [12] Y. Lu, Y. Dong, H. Jiang, Z. Wang, Z. Cao, S. Guo, T. Wang, T. Li, P.K. Liaw, Promising properties and future trend of eutectic high entropy alloys, *Scr. Mater.* 187 (2020) 202-209.

- [13] J. Duan, M. Wang, R. Huang, J. Miao, Y. Lu, T. Wang, T. Li, A novel high-entropy alloy with an exceptional combination of soft magnetic properties and corrosion resistance, *Sci. China Mater.* 66 (2023) 772–779.
- [14] P. Koželj, S. Vrtnik, A. Jelen, S. Jazbec, Z. Jagličić, S. Maiti, M. Feuerbacher, W. Steurer, J. Dolinšek, Discovery of a Superconducting High-Entropy Alloy, *Phys. Rev. Lett.* 113 (2014) 107001.
- [15] L. Sun, R.J. Cava, High-entropy alloy superconductors: Status, opportunities, and challenges, *Phys. Rev. Mater.* 3 (2019) 090301.
- [16] J. Kitagawa, S. Hamamoto, N. Ishizu, Cutting edge of high-entropy alloy superconductors from the perspective of materials research, *Metals* 10 (2020) 1078.
- [17] J. Kitagawa, Y. Mizuguchi, High-Entropy Alloy Superconductors: Exotic Properties, Applications and Materials Design, Springer, Singapore, (2024).
- [18] L. Zeng, L. Li, K. Li, R. Chen, H. Luo, Recent advances in high-entropy superconductors, *NPG Asia Mater* 16 (2024) 60.
- [19] J. Kitagawa, Y. Mizuguchi, T. Nishizaki, High critical current densities of body-centered cubic high-entropy alloy superconductors: recent research progress, *Eur. Phys. J. B* 98 (2025) 73.
- [20] J. Guo, H. Wang, F. von Rohr, Z. Wang, S. Cai, Y. Zhou, K. Yang, A. Li, S. Jiang, Q. Wu, R.J. Cava, L. Sun, Robust zero resistance in a superconducting high-entropy alloy at pressures up to 190 GPa, *Proc. Natl. Acad. Sci.* 114 (2017) 13144-13147.
- [21] M.R. Kasem, Y. Nakahira, H. Yamaoka, R. Matsumoto, A. Yamashita, H. Ishii, N. Hiraoka, Y. Takano, Y. Goto, Y. Mizuguchi, Robustness of superconductivity to external pressure in high-entropy-alloy-type metal telluride AgInSnPbBiTe_5 , *Sci. Rep.* 12 (2022) 7789.
- [22] S.-G. Jung, Y. Han, J.H. Kim, R. Hidayati, J.-S. Rhyee, J.M. Lee, W.N. Kang, W.S. Choi, H.-R. Jeon, J. Suk, T. Park, High critical current density and high-tolerance superconductivity in high-entropy alloy thin films, *Nat. Commun.* 13 (2022) 3373.

- [23] B.T. Matthias, Empirical relation between superconductivity and the number of valence electrons per atom, *Phys. Rev.* 97 (1955) 74–76.
- [24] T. Hattori, Y. Watanabe, T. Nishizaki, K. Hiraoka, M. Kakihara, K. Hoshi, Y. Mizuguchi, J. Kitagawa, Metallurgy, superconductivity, and hardness of a new high-entropy alloy superconductor Ti-Hf-Nb-Ta-Re, *J. Alloys Metallur. Syst.* 3 (2023) 100020.
- [25] T. Seki, H. Arima, Y. Kawasaki, T. Nishizaki, Y. Mizuguchi, J. Kitagawa, Effect of annealing in eutectic high-entropy alloy superconductor NbScTiZr, *J. Supercond. Nov. Magn.* 37 (2024) 1059–1068.
- [26] J. Kitagawa, H. Ueta, Y. Watanabe, T. Seki, Y. Mizuguchi, T. Nishizaki, Superconducting properties of eutectic high-entropy alloy superconductor NbScTiZr, *Mater. Today Commun.* 40 (2024) 109690.
- [27] M. Krnel, A. Jelen, S. Vrtnik, J. Luzar, D. Gačnik, P. Koželj, M. Wencka, A. Meden, Q. Hu, S. Guo, J. Dolinšek, The Effect of Scandium on the Structure, Microstructure and Superconductivity of Equimolar Sc-Hf-Nb-Ta-Ti-Zr Refractory High-Entropy Alloys, *Materials* 15 (2022) 1122.
- [28] J. Kim, S.-G. Jung, Y. Han, J.H. Kim, J.-S. Rhyee, S. Yeo, T. Park, Thermal-driven gigantic enhancement in critical current density of high-entropy alloy superconductors, *J. Mater. Sci. Technol.* 189 (2024) 60-67.
- [29] L. Gao, T. Ying, Y. Zhao, W. Cao, C. Li, L. Xiong, Q. Wang, C. Pei, J.-Y. Ge, H. Hosono, Y. Qi, Fishtail effect and the vortex phase diagram of high-entropy alloy superconductor, *Appl. Phys. Lett.* 120 (2022) 092602.
- [30] Y. Yamabe-Mitarai, K. Yanao, Y. Toda, I. Ohnuma, T. Matsunaga, Phase stability of Ti-containing high-entropy alloys with a bcc or hcp structure, *J. Alloys Compd.* 911 (2022) 164849.
- [31] N.R. Werthamer, E. Helfand, P.C. Hohenberg, Temperature and Purity Dependence of the Superconducting Critical Field, H_{c2} . III. Electron Spin and Spin-Orbit Effects, *Phys. Rev.* 147 (1966) 295-302.
- [32] S. Jangid, P.K. Meena, R.K. Kushwaha, S. Srivastava, P. Manna, P. Mishra, S. Sharma, R.P. Singh, Superconductivity with a high upper critical field in an equiatomic high-entropy alloy Sc-V-Ti-Hf-Nb, *Appl. Phys. Lett.* 124 (2024) 192602.

- [33] P. Sobota, B. Rusin, D. Gnida, R. Topolnicki, T. Ossowski, W. Nowak, A. Pikul, R. Idczak, New type of Ti-rich HEA superconductors with high upper critical field, *Acta Mater.* 285 (2025) 120666.
- [34] S. Marik, M. Varghese, K.P. Sajilesh, D. Singh, R.P. Singh, Superconductivity in equimolar Nb-Re-Hf-Zr-Ti high entropy alloy, *J. Alloys Compd.* 769 (2018) 1059-1063.
- [35] G. Kim, M.-H. Lee, J.H. Yun, P. Rawat, S.-G. Jung, W. Choi, T.-S. You, S. J. Kim, J.-S. Rhyee, Strongly correlated and strongly coupled s-wave superconductivity of the high entropy alloy $Ta_{1/6}Nb_{2/6}Hf_{1/6}Zr_{1/6}Ti_{1/6}$ compound, *Acta Mater.* 186 (2020) 250-256.
- [36] F. von Rohr, M.J. Winiarski, J.Tao, T.Klimczuk, R.J. Cava, Effect of electron count and chemical complexity in the Ta-Nb-Hf-Zr-Ti high-entropy alloy superconductor, *Proc. Natl. Acad. Sci.* 113 (2016) E7144.
- [37] N.K. Sarkar, C.L. Prajapat, P.S. Ghosh, N. Garg, P.D. Babu, S. Wajhal, P.S.R. Krishna, M.R. Gonal, R. Tewari, P.K. Mishra, Investigations on superconductivity in an equi-atomic disordered Hf-Nb-Ta-Ti-V high entropy alloy, *Intermetallics* 144 (2022) 107503.
- [38] L. Zeng, J. Zhan, M. Boubeche, K. Li, L. Li, P. Yu, K. Wang, C. Zhang, K. Jin, Y. Sun, H. Luo, Superconductivity in the bcc-Type High-Entropy Alloy TiHfNbTaMo, *Adv. Quantum Technol.* 6 (2023) 2300213.
- [39] H. Padamsee, J.E. Neighbor, C.A. Shiffman, Quasiparticle phenomenology for thermodynamics of strong-coupling superconductors, *J Low Temp Phys* 12 (1973) 387–411.
- [40] D.C. Johnston, Elaboration of the α -model derived from the BCS theory of superconductivity, *Supercond. Sci. Technol.* 26 (2013) 115011.
- [41] R.L. Peterson, Magnetization of anisotropic superconducting grains, *J. Appl. Phys.* 67 (1990) 6930–6933.
- [42] S.X. Dou, X.L. Wang, J. Horvat, D. Milliken, A.H. Li, K. Konstantinov, E.W. Collings, M.D. Sumption, H.K. Liu, Flux jumping and a bulk-to-granular transition in the magnetization of a compacted and sintered MgB_2 superconductor, *Physica C* 361 (2001) 79-83.

- [43] D. Larbalestier, A. Gurevich, D.M. Feldmann, A. Polyanskii, High- T_c superconducting materials for electric power applications, *Nature* 414 (2001) 368–377.
- [44] K. Komori, K. Kawagishi, Y. Takano, H. Fujii, S. Arisawa, H. Kumakura, M. Fukutomi, K. Togano, Approach for the fabrication of MgB_2 superconducting tape with large in-field transport critical current density, *Appl. Phys. Lett.* 81 (2002) 1047-1049.
- [45] T. Higuchi, S.I. Yoo, M. Murakami, Comparative study of critical current densities and flux pinning among a flux-grown $NdBa_2Cu_3O_y$ single crystal, melt-textured Nd-Ba-Cu-O, and Y-Ba-Cu-O bulks, *Phys. Rev. B* 59 (1999) 1514-1527.
- [46] I. Shigeta, T. Abiru, K. Abe, A. Nishida, Y. Matsumoto, Temperature and field dependence of magnetization of MgB_2 polycrystals, *Phys. C* 392-396 (2003) 359-363.
- [47] Q. Cai, Y. Liu, Z. Ma, H. Li, L. Yu, Variation of pinning mechanism and enhancement of critical current density in MgB_2 bulk containing self-generated coherent MgB_4 impurity, *Appl. Phys. Lett.* 103 (2013) 132601.
- [48] N. Ishizu, J. Kitagawa, New high-entropy alloy superconductor $Hf_{21}Nb_{25}Ti_{15}V_{15}Zr_{24}$, *Res. Phys.* 13 (2019) 102275.
- [49] Y. Harayama, J. Kitagawa, Superconductivity in Al-Nb-Ti-V-Zr multi-component alloy, *J. Supercond. Nov. Magn.* 34 (2021) 2787-2794.
- [50] J. Kitagawa, K. Hoshi, Y. Kawasaki, R. Koga, Y. Mizuguchi, T. Nishizaki, Superconductivity and hardness of the equiatomic high-entropy alloy $HfMoNbTiZr$, *J. Alloys Compd.* 924 (2022) 166473.
- [51] S. Vrtnik, P. Koželj, A. Meden, S. Maiti, W. Steurer, M. Feuerbacher, J. Dolinšek, Superconductivity in thermally annealed Ta-Nb-Hf-Zr-Ti high-entropy alloys, *J. Alloys Compd.* 695 (2017) 3530.
- [52] P. Sobota, R. Topolnicki, T. Ossowski, T. Pikula, A. Pikul, R. Idczak, Superconductivity in the high entropy alloy $(NbTa)_{0.67}(MoHfW)_{0.33}$, *Phys. Rev. B* 106 (2022) 184512.

- [53] R. Shu, X. Zhang, S. G. Rao, A. le Febvrier, P. Eklund, Effects of alloying and deposition temperature on phase formation and superconducting properties of TiZrTaNb-based high entropy-alloy films, *Appl. Phys. Lett.* 120 (2022) 151901.
- [54] B. Mitrović, H.G. Zarate, J.P. Carbotte, The ratio $2\Delta(0)/k_B T_c$, within Eliashberg theory, *Phys. Rev. B* 29 (1984) 184-189.
- [55] F. Marsiglio, J.P. Carbotte, Strong-coupling corrections to Bardeen-Cooper-Schrieffer ratios, *Phys. Rev. B* 33 (1986) 6141-6145.
- [56] P.B. Allen, R. C. Dynes, Transition temperature of strong-coupled superconductors reanalyzed, *Phys. Rev. B* 12 (1975) 905-922.
- [57] W.L. McMillan, Transition Temperature of Strong-Coupled Superconductors, *Phys. Rev.* 167 (1968) 331-344.
- [58] L. Zeng, X. Hu, M. Boubeche, K. Li, L. Li, P. Yu, K. Wang, C. Zhang, K. Jin, D.-X. Yao, H. Luo, Extremely strong coupling s-wave superconductivity in the medium-entropy alloy TiHfNbTa, *Sci. China Phys. Mech. Astron.* 66 (2023) 277412.
- [59] T. Xiong, W. Yang, S. Zheng, Z. Liu, Y. Lu, R. Zhang, Y. Zhou, X. Shao, B. Zhang, J. Wang, F. Yin, P. K. Liaw, X. Ma, Faceted Kurdjumov-Sachs interface-induced slip continuity in the eutectic high-entropy alloy, AlCoCrFeNi_{2.1}, *J. Mater. Sci. Technol.* 65 (2021) 216-227.
- [60] Y.-X. Zhuang, X.-L. Zhang, X.-Y. Gu, Effect of Annealing on Microstructure and Mechanical Properties of Al_{0.5}CoCrFeMo_xNi High-Entropy Alloys, *Entropy* 20 (2018) 812.